

# ***parahydrogen* Induced Polarization by Homogeneous Catalysis: Theory and Applications**

**Lisandro Buljubasich, María Belén Franzoni, and Kerstin Münnemann**

**Abstract** The alignment of the nuclear spins in *parahydrogen* can be transferred to other molecules by a homogeneously catalyzed hydrogenation reaction resulting in dramatically enhanced NMR signals. In this chapter we introduce the involved theoretical concepts by two different approaches: the well known, intuitive population approach and the more complex but more complete density operator formalism. Furthermore, we present two interesting applications of PHIP employing homogeneous catalysis. The first demonstrates the feasibility of using PHIP hyperpolarized molecules as contrast agents in  $^1\text{H}$  MRI. The contrast arises from the J-coupling induced rephasing of the NMR signal of molecules hyperpolarized via PHIP. It allows for the discrimination of a small amount of hyperpolarized molecules from a large background signal and may open up unprecedented opportunities to use the standard MRI nucleus  $^1\text{H}$  for, e.g., metabolic imaging in the future. The second application shows the possibility of continuously producing hyperpolarization via PHIP by employing hollow fiber membranes. The continuous generation of hyperpolarization can overcome the problem of fast relaxation times inherent in all hyperpolarization techniques employed in liquid-state NMR. It allows, for instance, the recording of a reliable 2D spectrum much faster than performing the same experiment with thermally polarized protons. The membrane technique can be straightforwardly extended to produce a continuous flow of a hyperpolarized liquid for MRI enabling important applications in natural sciences and medicine.

**Keywords** Homogeneous catalysis · Hyperpolarization · NMR signal enhancement · *parahydrogen* induced polarization · PHIP

*In honor of Prof. Hans W. Spiess*

## Contents

1	Introduction .....	34
2	Theory .....	35
2.1	Spin Isomers of the Hydrogen Molecule .....	35
2.2	Hydrogen Described from Statistical Mechanics .....	37
2.3	Preparation of Enriched <i>parahydrogen</i> .....	38
2.4	NMR Signal Enhancement with Enriched <i>parahydrogen</i> : A Population-Oriented Approach .....	40
2.5	Density Operator Formalism Applied to PHIP .....	42
2.6	Two Spin Systems .....	45
2.7	Larger Spin Systems and Hyperpolarization Transfer .....	54
3	Experimental Results and Applications .....	57
3.1	Catalytic Systems .....	57
3.2	The Model Compounds .....	59
3.3	PHIP Hyperpolarized Substances as Contrast Agents in $^1\text{H}$ MRI .....	60
3.4	Continuous Generation of a Hyperpolarized Fluid Using PHIP and Hollow Fiber Membranes .....	66
4	Conclusion .....	70
	References .....	71

## 1 Introduction

The hydrogenation of organic molecules with hydrogen enriched in the *para*-state creates a highly ordered spin state, resulting in the observation of largely enhanced NMR signals. In September 1987, Bowers and Weitekamp presented the first experimental verification of this effect. The title of the article, “*parahydrogen* and Synthesis Allow Dramatically Enhanced Nuclear Alignment” [1], inspired the popular name PASADENA for experiments where the hydrogenation reaction and the NMR spectrum acquisition are accomplished within the strong magnetic field of the spectrometer. Large *antiphase multiplets* in the  $^1\text{H}$  NMR spectra were reported. These signals appeared to be approximately 100 times larger than the intensity of the signals acquired with hydrogen in thermal equilibrium at room temperature.

A few months later in the same year an independent work by Eisenschmid et al., reported similarly enhanced spectra in two different hydrogenation reactions [2]. The title “Para Hydrogen Induced Polarization in Hydrogenation Reactions” represented the inception of the widespread acronym for all kind of experiments involving enriched *parahydrogen* i.e., PHIP.

In the next year (1988) another significant contribution was published by Pravica and Weitekamp [3], reporting the hydrogenation of styrene to ethylbenzene with enriched *parahydrogen*. The reaction was carried out at low magnetic field and subsequently the sample tube was adiabatically transported into the high field of the spectrometer to perform the NMR experiment. The resulting spectra markedly differed from the PASADENA counterpart. It displayed *two separate multiplets of opposite phases* for the two proton sites of the product molecule occupied by *parahydrogen*. They named this effect ALTADENA (Adiabatic Longitudinal Transport After Dissociation Engenders Net Alignment).

Since these initial publications the hydrogenation with *parahydrogen* has become a promising technique to boost the low sensitivity of NMR. Hence, during the last two and a half decades the technique was used in a wide range of applications encompassing: the investigation of the kinetics of inorganic reactions [4–6]; to explore heterogeneous reactions [7–9]; the observation of the spatial distribution of hyperpolarized gases by MRI [10, 11]; the use as contrast agent in MRI [12–15]; the transfer of the accomplished hyperpolarization using either suitable pulse sequences [16, 17], adiabatic field cycling [18] or transport through level avoiding crossing [19–21]; the study of long lived states [22–24] originating from *p*-H<sub>2</sub> [25–28] and, far from chemical applications, the particular *p*-H<sub>2</sub> spin state has been used in the context of quantum information processes [29–32].

This chapter does not represent a thorough review of the applications of *p*-H<sub>2</sub> and therefore the list of references presented here is necessarily incomplete. For a more complete discussion of the manifold applications of PHIP we refer the reader to the excellent review recently published by Green et al. [33] and to the contribution written by Duckett and Mewis within this book.

The emphasis of this chapter is on the theoretical aspects of PHIP, based mainly on a numerical approach, along with two experimental examples. In the theoretical part, first a short summary of the physics of *parahydrogen* is given, followed by a treatment of NMR with PHIP in a population model approach. Next, the density operator formalism is introduced and the major features of PASADENA and ALTADENA are explained in this context. Finally, hyperpolarization transfer to a third spin is treated. In the experimental part we include two practical applications of PHIP. The first example shows the potential use of PHIP to create a novel contrast in <sup>1</sup>H MRI. The second example is related to the achievement of continuous hyperpolarization with PHIP by means of hollow fiber membranes. Two model compounds are presented: one is soluble in water while the other one is soluble in organic solvents.

## 2 Theory

### 2.1 Spin Isomers of the Hydrogen Molecule

Among the applications of quantum mechanics in chemistry, one of the first triumphs was the successful calculation of the structure of very simple molecules. The simplest of all molecules is the hydrogen molecule-ion, H<sub>2</sub><sup>+</sup>, composed of two hydrogen nuclei and one electron. Within a year after the development of quantum mechanics, a description of the normal state of the hydrogen molecule-ion was obtained, in complete agreement with experiments. The next molecule, in terms of simplicity, is the hydrogen molecule. The contribution by Heitler and London in 1927 [34] is considered as the inception of the application of quantum mechanics to problems of molecular structure. However, the full treatment is rather complicated.

We include here only a short summary of the quantum mechanical properties of the hydrogen molecule (a detailed treatment can be found, for instance, in [35]).

The total wave function of the hydrogen molecule can be represented as the product of five functions:

$$\psi = \psi_e^{\text{orb}} \psi_e^s \psi_n^{\text{vib}} \psi_n^{\text{rot}} \psi_n^s, \quad (1)$$

describing the orbital motion of electrons, the electron spin state, the vibrational state of the nuclei, the rotational motion of the nuclei, and the nuclear spin state, respectively [35]. The first wave function, corresponding to the electronic ground state,  $^1\Sigma_g^+$ , is symmetric with respect to the electrons [36], the second is antisymmetric, and the rest are independent of the electrons' variables and symmetric. This makes the entire wave function antisymmetric in the two electrons, as required by Pauli's principle [37]. On the other hand,  $\psi_e^{\text{orb}}$  is symmetric with respect to the nuclei [35];  $\psi_e^s$  is also symmetric because it is independent of nuclear coordinates. As the positions of both nuclei can be interchanged without affecting the vibrational state, the third function is symmetric. The overall symmetry of the total wave function depends, thus, on the symmetry of the product  $(\psi_n^{\text{rot}} \psi_n^s)$ .

Interchanging the two nuclei transforms  $\psi_n^{\text{rot}}$  to [35, 37]

$$P_{12}(\psi_n^{\text{rot}}) = (-1)^J \psi_n^{\text{rot}}, \quad (2)$$

where  $P_{12}$  represents the permutation operator that interchanges the nuclei's positions and  $J$  is the rotational quantum number. Hence, the rotational wave function is symmetric for even rotational states ( $J = 0, 2, 4, \dots$ ) and antisymmetric for odd rotational states ( $J = 1, 3, 5, \dots$ ). The nuclear spin function can be either symmetric or antisymmetric. Following the rules for adding angular momenta in quantum mechanics, it can be shown that the combination of the two spins corresponding to each nucleus gives four possible functions. They can be written as linear combinations of the direct product of the two possible spin orientations for each single spin, i.e., as

$$\begin{aligned} \psi_{+1}^T &= |\alpha\alpha\rangle, \\ \psi_0^T &= \frac{1}{\sqrt{2}}(|\alpha\beta\rangle + |\beta\alpha\rangle), \\ \psi_{-1}^T &= |\beta\beta\rangle, \\ \psi_0^S &= \frac{1}{\sqrt{2}}(|\alpha\beta\rangle - |\beta\alpha\rangle). \end{aligned} \quad (3)$$

The functions are grouped according to their total angular momentum number. The first three functions have total spin  $S = 1$  (with the  $z$ -projection indicated in the subindices) while the fourth function possesses total spin  $S = 0$ . They are commonly termed as triplet and singlet, respectively; the triplet is symmetric on the nuclei and the singlet is antisymmetric.

According to Pauli's principle, the symmetric rotational functions must be combined with the singlet nuclear function, whereas each antisymmetric rotational function has to be associated with the three symmetric spin functions, to yield a total wave function being antisymmetric on the nuclei. Hence, there are two hydrogen isomers, one called *parahydrogen* ( $p\text{-H}_2$ ), having an antisymmetric nuclear spin function and existing only in even rotational states, and the other called *orthohydrogen* ( $o\text{-H}_2$ ), having a symmetric nuclear spin function and existing only in the odd rotational states. Moreover, as the transition between even and odd rotational states implies a transition between singlet and triplet nuclear spin states, which is symmetry forbidden, the proportion of *ortho*- and *para*hydrogen is quasistable at any given temperature. It was Dennison, back in 1927, who showed that the interconversion of  $o\text{-H}_2$  to  $p\text{-H}_2$  is extremely slow [38]. Two years later it was discovered by Bonhoeffer and Harteck [39] that catalysts such as charcoal accelerate the achievement of thermodynamic equilibrium, thus permitting the fast modification of the ratio  $o\text{-H}_2/p\text{-H}_2$  by cooling or heating the gas.

## 2.2 Hydrogen Described from Statistical Mechanics

In order to quantitatively describe the state of an ensemble of hydrogen molecules it is necessary to resort to statistical mechanics. The partition function of the system [78] reads

$$Z = \sum_i d_i e^{-E_i/kT}, \quad (4)$$

where  $d_i$  represents the degeneracy of the  $i$ th energy level  $E_i$ ,  $k$  is the Boltzmann constant, and  $T$  the absolute temperature. Vibrational and electronic modes are not activated in hydrogen gas at room temperature or below [40] and therefore only the vibrational and electronic ground states are populated and contribute to the partition function. Thus, we need to focus only on the rotational and nuclear spin states. Using the Born–Oppenheimer rigid rotor approximation, the rotational energy levels can be expressed as

$$E_J = J(J + 1) \frac{\hbar^2}{2I}, \quad (5)$$

where  $I$  is the moment of inertia of the hydrogen molecule [35]. It can be clearly seen from Eq. (5) that the energy gap increases with the quantum number  $J$ , being the first (i.e.,  $E_{J=0} \rightarrow E_{J=1}$ ) [40]:

$$\Delta E_{J=0 \rightarrow J=1} = h \times 3.7 \times 10^{12} \text{ Hz}. \quad (6)$$

The energy differences between nuclear states are much smaller (in the order of Hz) and therefore the partition function can further be simplified by considering only the rotational energy levels with the extra degeneracy produced by the nuclear states.

The rotational energy levels are populated according to the Boltzmann equilibrium distribution, with the population of each state given by

$$P_J = \frac{1}{Z} d_J d_S e^{-E_J/kT}. \quad (7)$$

The factor  $d_J$  corresponds to the degeneracy of the rotational states, which is  $(2J + 1)$  in the absence of electric and magnetic fields, and  $d_S$  is the degeneracy due to nuclear spin states. The population of each level can be recast as

$$P_J = \frac{1}{Z} (2J + 1) d_S e^{-J(J+1)\theta_r/T}, \quad (8)$$

where the *rotational temperature* has been defined as  $\theta_r = \hbar^2/2IK$  [30, 41].

In Fig. 1a, b the populations of the first six rotational levels are plotted against the absolute temperature for *parahydrogen* ( $J = 0, 2, 4$ ) and *orthohydrogen* ( $J = 1, 3, 5$ ), respectively. At very low temperatures ( $T < 20$  K) only the level corresponding to  $J = 0$  is observably populated and, consequently, almost 100% of the hydrogen molecules in the gas will be in the *para*-state. As the temperature increases, more molecules initially at the lowest level populate the next levels. At room temperature the first four states are substantially more populated and contribute to the *para* and *orthohydrogen* fractions.

The amount of *parahydrogen* at any temperature in thermal equilibrium is obtained by accounting the populations of all rotational levels with even quantum number:

$$N_{para} = \frac{1}{Z} \sum_{J=\text{even}} (2J + 1) e^{-J(J+1)\theta_r/T}. \quad (9)$$

This curve is displayed in Fig. 1c. The dashed vertical line points out the conversion temperature of  $T = 77$  K, the boiling temperature of nitrogen, where the gas is comprised of equal amounts of *p*-H<sub>2</sub> and *o*-H<sub>2</sub>. At room temperature the fraction of *p*-H<sub>2</sub> is  $\sim 1/4$ .

### 2.3 Preparation of Enriched parahydrogen

The plot in Fig. 1c suggests the method of enriching hydrogen in the *para*-state. As stated above, the thermal equilibrium in an ensemble of hydrogen molecules involves transitions between nuclear states with different symmetry. Such

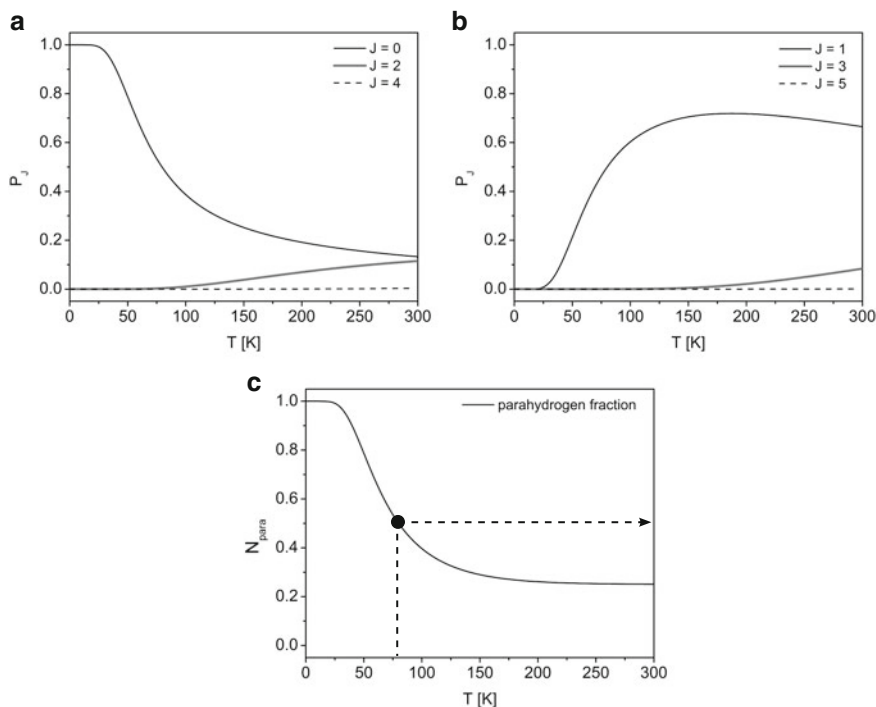


**Fig. 1** (a) Population of the rotational levels  $J = 0, 2, 4$ , corresponding to *parahydrogen*; (b) same as in (a) for *orthohydrogen* ( $J = 1, 3, 5$ ); (c) *parahydrogen* fraction present in an ensemble of hydrogen molecule in the gas phase at thermal equilibrium vs temperature. The dashed line depicts the nitrogen boiling temperature, i.e., 77 K

transitions are possible in the presence of perturbations involving the nuclear spins, but these perturbations are extremely small in pure hydrogen. In other words, it is possible to have hydrogen gas for a reasonably long time out of thermal equilibrium (ranging from days to weeks, depending on the container). In contact with a catalyst like charcoal, however, the paramagnetic centers make the transitions more likely, causing thermal equilibrium to occur very rapidly.

If a volume of hydrogen is cooled with, for instance, liquid nitrogen in the presence of a charcoal catalyst, it will quickly reach the situation marked with a dot in Fig. 1c. If the catalyst is removed afterwards and the gas is warmed up to room temperature the *parahydrogen* amount is ~50%, in contrast to the ~25% expected in thermal equilibrium at the same temperature.

Note that if the cooling process is performed at temperatures lower than 20 K the gas will contain almost 100% *parahydrogen*.

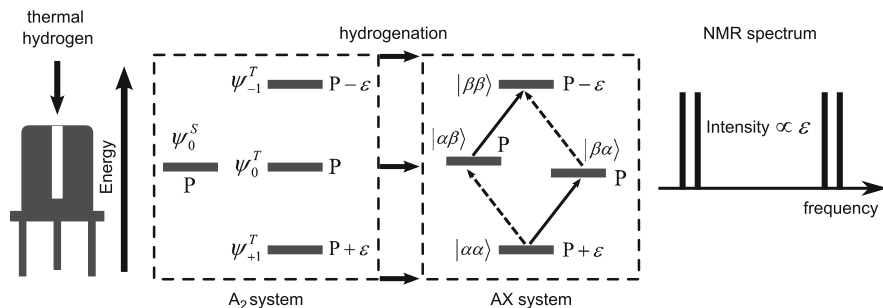


**Fig. 2** NMR spectrum after a hydrogenation with natural abundance  $p$ -H<sub>2</sub>. The four eigenstates in the initial A<sub>2</sub> spin system are equally populated. The transferred protons form an AX system in the target molecule

## 2.4 NMR Signal Enhancement with Enriched parahydrogen: A Population-Oriented Approach

In order to understand intuitively the mechanism leading to the NMR signal enhancement when performing a hydrogenation reaction with hydrogen enriched in the *para*-state, it is useful to analyze the different NMR spectra focusing on the levels' population differences. This is the most utilized approach described in several publications [36, 42, 43], and we will shortly summarize it here for the sake of completeness. We will focus our attention on a homogeneous hydrogenation reaction where the hydrogen nuclei are transferred *pairwise* to a target molecule. The catalyst used for the hydrogenation reaction is crucial in these processes, because the enhanced signal arises only from those reactions capable to preserve the singlet symmetry of  $p$ -H<sub>2</sub>. We assume that the  $p$ -H<sub>2</sub> protons in the target molecule form, at high fields, an AX system isolated from the rest of the molecule. An example of such a reaction is the hydrogenation of propiolic acid- $d_2$  catalyzed by [Rh(COD)dppb]<sup>+</sup>BF<sub>4</sub><sup>-</sup> [42].

When performing the reaction with thermal hydrogen at room temperature (i.e., hydrogen at thermal equilibrium) the NMR spectrum is independent of whether the reaction occurs at low or high magnetic field. We assume that the gas is introduced in the bore and the reaction is carried out inside the magnet, as depicted in Fig. 2. The hydrogen forms an A<sub>2</sub> spin system described by the eigenfunctions of Eq. (3), and the four eigenstates are equally populated ( $P = 0.25$ ) out of the magnet. Inside the magnet the energy levels are accordingly modified and the population distribution follows the Boltzmann distribution, changing by an amount known as the Boltzmann factor,  $\epsilon = \hbar\gamma B_0/kT_{\text{exp}}$ , of the order of  $10^{-5}$  for protons at room temperature and ordinary magnetic fields. After the reaction with thermal hydrogen, the transferred protons become an AX system described by the eigenfunctions of the Zeeman basis [44],  $B = \{|\alpha\alpha\rangle, |\alpha\beta\rangle, |\beta\alpha\rangle, |\beta\beta\rangle\}$ . The corresponding NMR spectrum consists of four lines of identical intensities, proportional to the Boltzmann factor, as pictorially shown in Fig. 2.



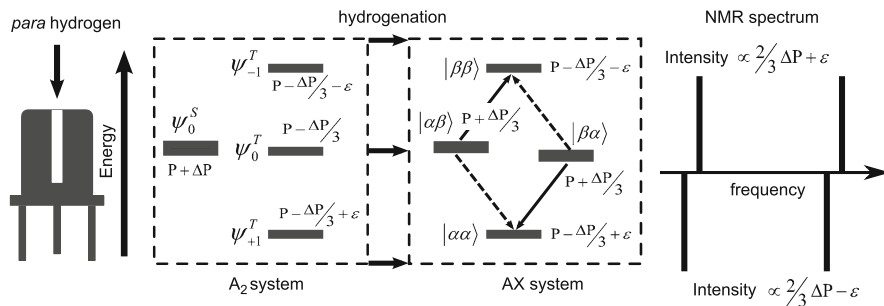


**Fig. 3** PASADENA experiment for an AX spin system. The chemical reaction with hydrogen gas enriched in the *para*-state occurs inside the magnet. The *p*-H<sub>2</sub> enrichment is evidenced in the overpopulation of the singlet state, eigenstate of the A<sub>2</sub> system

In contrast, if the experiment is performed with hydrogen enriched in the *para*-state, the final result strongly depends on the magnetic field at which the reaction is accomplished. There are two main procedures distinguished in the literature: PASADENA, where the gas is transported to the magnet and the reaction is carried out at the same magnetic field strength at which the NMR experiment is performed (typically high magnetic fields [1, 45]), and ALTADENA, where the reaction is conducted at low field and the product is subsequently moved into the magnet to start the NMR experiment.

Let us consider hydrogen gas with an excess of population in the *para*-state denoted as  $\Delta P$ , ranging from 0 (thermal hydrogen) to  $3P$  (pure *para*hydrogen). Then the total population of the singlet and triplet states are  $P + \Delta P$  and  $P - \Delta P$ , respectively. Inside the magnet the populations of the levels corresponding to  $\psi_{+1}^T$  and  $\psi_{-1}^T$  are corrected by  $\epsilon$  due to the Boltzmann equilibrium distribution (see Fig. 3).

Right after the reaction the excess population of  $\psi_0^S$  equally populates the levels labeled as  $|\alpha\beta\rangle$  and  $|\beta\alpha\rangle$  in the product molecule. As a result, the NMR spectrum presents two antiphase doublets with intensities of the order of  $\frac{2}{3}\Delta P \pm \epsilon$ , as shown in Fig. 3. Note that  $\Delta P$  is close to unity, whereas  $\epsilon \sim 10^{-5}$ , demonstrating the large signal enhancement that can be accomplished by hyperpolarization. The intensity of the PASADENA spectrum is, for the case treated here and neglecting relaxation, between four and five orders of magnitude larger than the intensity obtained in the reaction with thermal hydrogen.

If, alternatively, the reaction is performed at low field (typically at the earth field) and the sample is adiabatically transported to the magnet in the sense that the initial eigenstate  $\psi_0^S$  follows the corresponding eigenstates for each magnetic field, then the total excess of population initially in  $\psi_0^S$  ends up in  $|\beta\alpha\rangle$ , the eigenstate of the AX system. Consequently, the NMR spectrum looks different compared to the PASADENA spectrum, displaying only two peaks with opposite phases which have twice the intensities of the PASADENA peaks (Fig. 4).

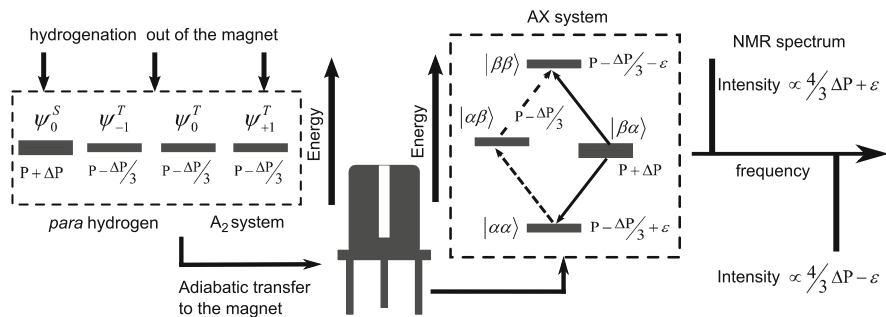


**Fig. 4** ALTADENA experiment for an AX spin system. The chemical reaction is performed outside the magnet, followed by an adiabatic transport of the sample into the NMR observation field

The population oriented explanation helps in understanding the major features of PHIP experiments, such as the shape of the spectra and the signal enhancement. However, the analysis becomes extremely cumbersome when trying to extend it to strongly coupled (e.g., AB or  $A_2$ ) and larger spin systems. A more general treatment of PHIP, applicable to arbitrary spin systems, can be performed by using the enormous power of the density matrix formalism to calculate NMR signals.

## 2.5 Density Operator Formalism Applied to PHIP

The density operator formalism is commonly used in the NMR community to calculate signals after the application of a given r.f. pulse sequence [44, 46]. We briefly describe here the formalism applied to the calculation of experiments involving hydrogenations with *parahydrogen*.

The formal definition of the density operator is

$$\rho = \sum_i w_i |\psi_i\rangle \langle \psi_i|, \quad (10)$$

where  $w_i$  represents the fraction of the  $i$ th state in the ensemble. In the absence of an external magnetic field the natural basis to express the matrix associated to the density operator of a generic ensemble of hydrogen molecules is:

$$B' = \{\psi_{+1}^T, \psi_0^T, \psi_{-1}^T, \psi_0^S\}, \quad (11)$$

since the vectors are the eigenvectors [see Eq. (3)]. However, it is usually preferred to express the density operator in the Zeeman basis (alternatively called computational basis),  $B = \{|\alpha\alpha\rangle, |\alpha\beta\rangle, |\beta\alpha\rangle, |\beta\beta\rangle\}$ . The components of the density operator are in this basis:

$$\begin{aligned}
 |\psi_{+1}^T\rangle\langle\psi_{+1}^T| &= \begin{pmatrix} 1 & 0 & 0 & 0 \\ 0 & 0 & 0 & 0 \\ 0 & 0 & 0 & 0 \\ 0 & 0 & 0 & 0 \end{pmatrix}, & |\psi_0^T\rangle\langle\psi_0^T| &= \frac{1}{2} \begin{pmatrix} 0 & 0 & 0 & 0 \\ 0 & 1 & 1 & 0 \\ 0 & 1 & 1 & 0 \\ 0 & 0 & 0 & 0 \end{pmatrix}, \\
 |\psi_{-1}^T\rangle\langle\psi_{-1}^T| &= \begin{pmatrix} 0 & 0 & 0 & 0 \\ 0 & 0 & 0 & 0 \\ 0 & 0 & 0 & 0 \\ 0 & 0 & 0 & 1 \end{pmatrix}, & |\psi_0^S\rangle\langle\psi_0^S| &= \frac{1}{2} \begin{pmatrix} 0 & 0 & 0 & 0 \\ 0 & 1 & -1 & 0 \\ 0 & -1 & 1 & 0 \\ 0 & 0 & 0 & 0 \end{pmatrix}.
 \end{aligned} \tag{12}$$

The use of this basis permits the straightforward decomposition in product operators [44, 47], as

$$\begin{aligned}
 |\psi_{+1}^T\rangle\langle\psi_{+1}^T| &= \frac{1}{4}\mathbb{I} + \frac{1}{2}(I_1^z + I_2^z + 2I_1^z I_2^z), \\
 |\psi_0^T\rangle\langle\psi_0^T| &= \frac{1}{4}\mathbb{I} + \frac{1}{2}(2I_1^x I_2^x + 2I_1^y I_2^y - 2I_1^z I_2^z), \\
 |\psi_{-1}^T\rangle\langle\psi_{-1}^T| &= \frac{1}{4}\mathbb{I} + \frac{1}{2}(-I_1^z - I_2^z + 2I_1^z I_2^z), \\
 |\psi_0^S\rangle\langle\psi_0^S| &= \frac{1}{4}\mathbb{I} + \frac{1}{2}(-2I_1^x I_2^x - 2I_1^y I_2^y - 2I_1^z I_2^z).
 \end{aligned} \tag{13}$$

Slightly modifying notation, we define one density operator for pure *orthohydrogen* and one density operator for pure *parahydrogen*, setting in Eq. (10)  $w = 1/3$  for every component of *o*-H<sub>2</sub> and  $w = 1$  for *p*-H<sub>2</sub>, to obtain an accurate normalization. Thus,

$$\begin{aligned}
 \rho^{ortho} &= \frac{1}{3}\{|\psi_{+1}^T\rangle\langle\psi_{+1}^T| + |\psi_0^T\rangle\langle\psi_0^T| + |\psi_{-1}^T\rangle\langle\psi_{-1}^T|\} = \frac{1}{4}\mathbb{I} + \frac{1}{3}(I_1^x I_2^x + I_1^y I_2^y + I_1^z I_2^z), \\
 \rho^{para} &= |\psi_0^S\rangle\langle\psi_0^S| = \frac{1}{4}\mathbb{I} - (I_1^x I_2^x + I_1^y I_2^y + I_1^z I_2^z).
 \end{aligned} \tag{14}$$

The above expressions can be more compactly written as

$$\begin{aligned}
 \rho^{ortho} &= \frac{1}{4}\mathbb{I} + \frac{1}{3}\mathbf{I}_1 \cdot \mathbf{I}_2, \\
 \rho^{para} &= \frac{1}{4}\mathbb{I} - \mathbf{I}_1 \cdot \mathbf{I}_2.
 \end{aligned} \tag{15}$$

Denoting by  $\rho^{\text{hydr}}$  the density matrix of an ensemble of hydrogen molecules with an arbitrary fraction of *parahydrogen* represented by  $N_{para}$ , we obtain

$$\rho^{\text{hydr}} = (1 - N_{para})\rho^{ortho} + N_{para}\rho^{para} = \frac{1}{4}\mathbb{I} - \xi\mathbf{I}_1 \cdot \mathbf{I}_2 - \frac{\xi}{4}(I_1^z + I_2^z), \tag{16}$$

where  $\xi \equiv (4N_{para} - 1)/3$ . The third factor above, associated with thermal equilibrium in the presence of a strong magnetic field, was added for completeness. The fraction

$N_{para}$  depends on the temperature at which the hydrogen is enriched, as shown in Fig. 1c. Note that  $N_{para} = \frac{1}{4}$  at room temperature and therefore the second term of the right-hand side of Eq. (16) vanishes (i.e.,  $\xi = 0$ ). Consequently, the term associated with the Boltzmann factor will dominate, recovering the density matrix for a two spin system in thermal equilibrium at that temperature. On the other hand, at low temperatures, typically  $T < 20$  K,  $N_{para} \approx 1$  (i.e.,  $\xi = 1$ ), the density operator is dominated by the second term on the right side of Eq. (16), and the thermal factor can be safely neglected.

In PHIP experiments the hydrogen gas is always cooled down and the *parahydrogen* state is sufficiently enriched such that  $1/2 \leq N_{para} \leq 1$ . Therefore the thermal equilibrium is usually neglected in Eq. (16). For the rest of the chapter, and without loss of generality, we will set  $\xi \equiv 1$  in the calculations. The overall behavior of the NMR signals will still be reproduced except for a scaling factor  $\xi$  influencing the intensity of the NMR spectra.

The initial density operator  $\rho^{para}$  is proportional to the term  $\mathbf{I}_1 \cdot \mathbf{I}_2$  [see Eq. (15)] which is invariant under rotations and consequently no NMR observable magnetization is achieved in principle. However, if the two protons of the same *p*-H<sub>2</sub> molecule are transferred pairwise to a molecule during a hydrogenation reaction, the thermal equilibrium density operator of the product molecule will be perturbed. Assuming that the precursor of the target molecule (educt) consists of  $N$  spins-1/2, the thermal equilibrium density operator in the high temperature approximation can be expressed as [44, 46, 48]

$$\rho^{ed}(0) = \frac{1}{2^N} \mathbb{I} - \frac{1}{2^N} \sum_{k=1}^N \varepsilon_k I_k^z, \quad (17)$$

where  $\mathbb{I}$  is the identity operator with the proper dimensions, and  $\varepsilon_k$  the Boltzmann factor of the  $k$ th nucleus (to include the possibility of heteronuclei). This is the density operator for the educt molecule just before the beginning of the reaction. The density operator for the product molecule at  $t = 0$  is constructed as usual:

$$\rho^{pr}(0) = \rho^{hydr} \otimes \rho^{ed}(0). \quad (18)$$

The symbol  $\otimes$  denotes the direct product of the matrices associated with the density operators. A very useful approximation, commonly introduced to simplify the calculations, consists in neglecting the Boltzmann terms in Eq. (17), invoking the argument given above, in Eq. (16) [49, 50]. Therefore the product's density operator just after the hydrogenation results in

$$\rho^{pr}(0) = \rho^{hydr}(0) \otimes \frac{1}{2^N} \mathbb{I}. \quad (19)$$

Immediately after the reaction, there evolves according to the Liouville–von Neumann equation,

$$\frac{d\rho^{pr}(t)}{dt} = -i[H^{pr}, \rho^{pr}(t)], \quad (20)$$

where  $H^{\text{pr}}$  is the spin Hamiltonian of the product molecule. The Hamiltonian can, in general, be written as [44, 46]

$$H^{\text{pr}} = 2\pi \sum_{k=1}^N \nu_k I_k^z + 2\pi \sum_{k,l;k}^N J_{k,l} \mathbf{I}_k \cdot \mathbf{I}_l. \quad (21)$$

The terms on the right-hand side of the equation represent the *chemical shift* and the *J-coupling* interactions, respectively. For this time-independent Hamiltonian the formal solution of Eq. (20) is [46, 51]

$$\rho^{\text{pr}}(t) = e^{(-iH^{\text{pr}}t)} \rho^{\text{pr}}(0) e^{(+iH^{\text{pr}}t)}. \quad (22)$$

This description is appropriate for the time evolution of a single reacting molecule. However, in order to treat the whole hydrogenation process, an ensemble of molecules must be considered. Let us assume that the chemical reaction is carried out in a total reaction time  $t_r$ . Several molecules in the ensemble will react at different times  $\tau_i$ , distributed in the time interval  $0 < \tau_i < t_r$ , prior to the beginning of the NMR experiment. Thus, at the time of the NMR measurement, there will be an ensemble of density operators  $\rho_i^{\text{pr}}$  which have individually evolved for different time periods  $t_r - \tau_i$ . If the reaction takes longer than the characteristic times of any internal evolution, i.e.,  $t_r \gg 1/\nu_k, 1/J_{k,l}$  for all  $\nu_k$  and  $J_{k,l}$  present in the Hamiltonian, the average density operator can be obtained by time averaging [4, 43]:

$$\bar{\rho}^{\text{pr}}(t_r) = \frac{1}{t_r} \int_{t=0}^{t_r} \rho^{\text{pr}}(t) dt. \quad (23)$$

As a consequence of the reaction and subsequent evolution, hyperpolarization can spread from the *parahydrogen* to the rest of the molecule, depending only on the molecular Hamiltonian [4, 49]. Under favorable conditions even the signals of heteronuclei can be significantly enhanced by hyperpolarization transfer [14, 50].

## 2.6 Two Spin Systems

The time evolution of the density operator along with the different features of the PHIP NMR spectra is revised here for the case where the *parahydrogen* protons are deposited into two magnetically inequivalent sites. It is further assumed that there exists *no* coupling to the rest of the molecule. Thus the transferred protons will form either a weakly coupled AX spin system or a strongly coupled AB spin system depending on the comparison between their coupling strength and their chemical shift difference. If both spins are chemically equivalent, i.e., forming an  $A_2$  spin system, the former *parahydrogen* protons maintain the singlet nature which is NMR silent, and therefore it is excluded from this treatment [21]. It is important to note that the case  $AA'$  is nonexistent in an isolated two spin system.

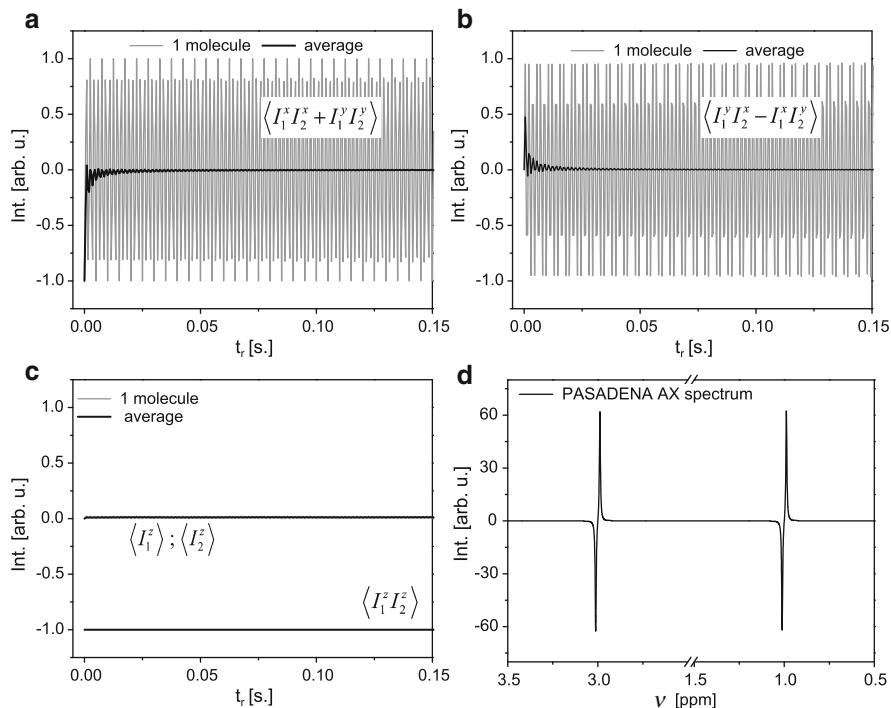


**Fig. 5** PASADENA AX system. Evolution of the expectation values: (a)  $ZQ_x$ ; (b)  $ZQ_y$ ; (c)  $I_1^z$ ,  $I_2^z$ , and  $I_1^z I_2^z$ . The results for one single molecule (*gray*) and for the ensemble average (*black*) are shown. Note that only the longitudinal order expectation value remains different from zero in the ensemble. (d) Simulated spectrum

### 2.6.1 PASADENA in an AX Spin System

We consider here a reaction with enriched *parahydrogen* performed at high magnetic field, such that the protons form an isolated AX spin system in the product molecule. Before the reaction, the density operator is  $\rho^{\text{pr}}(0) = \mathbb{I}/4 - \mathbf{I}_1 \cdot \mathbf{I}_2$ . The plots in Fig. 5 display the evolution of the density operator's components under the high field Hamiltonian during the reaction, for a single molecule  $\rho^{\text{pr}}(t_r)$  (gray line), superimposed with the ensemble average evolution  $\bar{\rho}^{\text{pr}}(t_r)$  (black line). The contribution of the identity operator is neglected.

The expectation value of the zero-quantum operator,  $ZQ_x = -(I_1^x I_2^x + I_1^y I_2^y)$  [4], initially present in the density operator  $\rho^{\text{pr}}(0)$ , oscillates and produces the zero quantum term  $ZQ_y = (I_1^y I_2^x - I_1^x I_2^y)$  that oscillates as well with zero mean expectation value, as shown in Fig. 5a, b. However, the time average of both expectation values vanishes after sufficiently long reaction times. The expectation value of the longitudinal order term  $I_1^z I_2^z$ , on the other hand, does not evolve and the time average yields exactly the initial value. The terms  $\langle I_1^z \rangle$  and  $\langle I_2^z \rangle$  maintain their zero-value during the process (Fig. 5c).

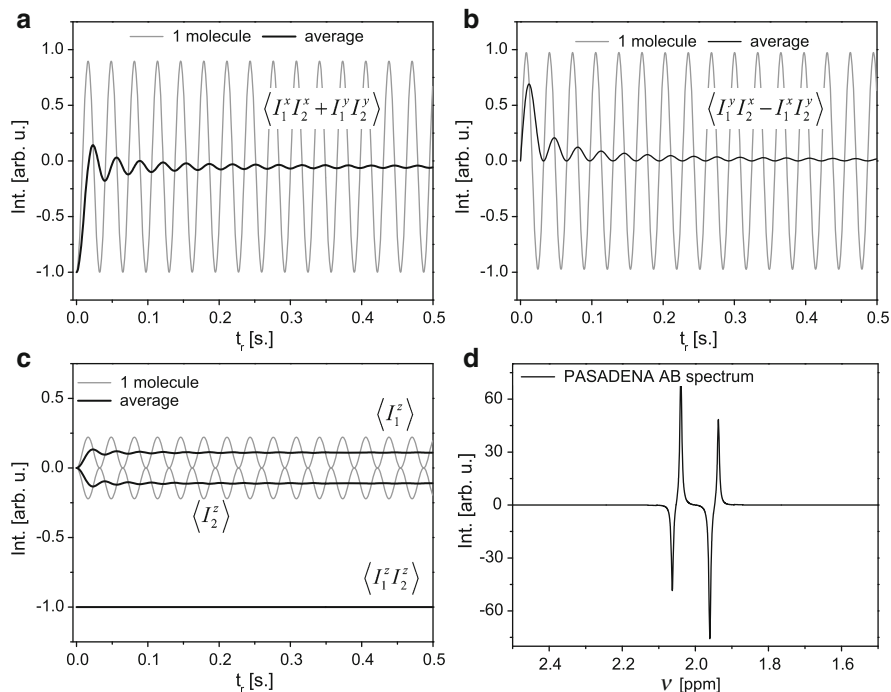


**Fig. 6** PASADENA AB spin system. Evolution of the expectation values for the operators: (a)  $ZQ_x$ ; (b)  $ZQ_y$ ; (c)  $I_1^z$ ,  $I_2^z$ , and  $I_1^z I_2^z$ . The results for one single molecule (*gray*) and for the ensemble average (*black*) are shown. The polarization expectation values also remain different from zero in the ensemble. (d) Simulated spectrum

In order to clarify the notation, it is convenient to introduce the variable  $t_f$  to indicate the reaction time which is long enough to fulfill the condition:  $t_f > 1/\nu_k$ ,  $1/J_{k,l}$  for all  $\nu_k$  and  $J_{k,l}$ . Then we can write  $\bar{\rho}^{\text{Pr}}(t_f) = \mathbb{I}/4 - I_1^z I_2^z$ , which results, after a  $45^\circ$  radiofrequency pulse, in the spectrum shown in Fig. 5d. The following numerical data were introduced in the calculations:  $B_0 = 7 \text{ T}$ ,  $\Delta\nu = 2 \text{ ppm}$  and  $J_{1,2} = 7 \text{ Hz}$ . Note that the spectrum's shape is similar to that predicted by the population approach (see Fig. 3).

## 2.6.2 PASADENA in an AB Spin System

If the chemical shift difference between the *parahydrogen* protons in the product molecule is not much larger than  $J_{1,2}$ , they form an isolated AB spin system. The smaller chemical shift difference reduces the oscillation frequency of the zero quantum expectation values  $\langle ZQ_x \rangle$  and  $\langle ZQ_y \rangle$  and consequently it takes longer to reach the steady state, as can be seen in Fig. 6a, b (i.e.,  $t_f > \frac{1}{\Delta\nu}$ ). The longitudinal order is conserved in the reaction as before, but the evolution of the zero-quantum

terms generates non-zero average polarization in both sites,  $\langle I_1^z \rangle$  and  $\langle I_2^z \rangle$  (Fig. 6c) [52]. The average density operator after reaching the steady state differs considerably from its counterpart in the AX system:  $\bar{\rho}^{\text{pr}}(t_f) = \mathbb{I}/4 - I_1^z I_2^z + 0.1(I_1^z - I_2^z)$ . The corresponding spectrum also presents the characteristic anti-phase doublets, with slightly different intensities. The spectrum was calculated setting:  $B_0 = 7 \text{ T}$ ,  $\Delta\nu = 0.1 \text{ ppm}$ , and  $J_{1,2} = 7 \text{ Hz}$ .

Although the PASADENA-AX and PASADENA-AB NMR spectra from Figs. 5, 6 do not differ substantially, it is important to note that in both cases a  $45^\circ$  pulse was employed before signal calculation. In general, a  $\theta$  pulse acts differently on longitudinal order operators and polarization operators. Typically, a  $90^\circ$  pulse applied to a polarization operator ( $I_1^z$  or  $I_2^z$ ) produces maximum signal while being applied to a longitudinal order term ( $I_1^x I_2^z$ ), giving zero signal. On the other hand, a  $45^\circ$  pulse produces maximum signal on longitudinal order operators and only a fraction of the maximum ( $\sqrt{2}/2$ ) on polarization operators. Therefore, the PASADENA-AB spectrum shows a strong shape dependence on the radiofrequency pulse while the PASADENA-AX spectrum is just rescaled [26, 43].

### 2.6.3 General PASADENA

We can make the situations treated above more general by considering the former *parahydrogen* protons being transferred to a molecule where they form an isolated two spin system described by  $\zeta = \Delta\nu/J$ . In the lower limit case,  $\zeta = 0$ , the spins form an  $A_2$  system. The initial density operator commutes with the Hamiltonian and, consequently, it does not evolve, preserving the magnetic equivalence during the reaction  $\bar{\rho}_{(\zeta=0)}^{\text{pr}}(t_f) = \mathbb{I}/4 - \mathbf{I}_1 \cdot \mathbf{I}_2$  and remaining NMR silent. From the calculations it can be observed that, for any  $\zeta \neq 0$ , the steady state averaged density operator can be expressed as  $\bar{\rho}_{(\zeta \neq 0)}^{\text{pr}}(t_f) = \mathbb{I}/4 - \eta_{\text{ZQ}_x}(I_1^x I_2^x + I_1^y I_2^y) - I_1^z I_2^z + \eta_{\text{pol}}(I_1^z - I_2^z)$ . Analytical expressions for  $\eta_{\text{ZQ}_x}$  and  $\eta_{\text{pol}}$  can be found, for instance, in [4, 43]. We maintain here our numerical treatment. The latter expression can be rearranged (noting that  $\mathbf{I}_1 \cdot \mathbf{I}_2 = I_1^x I_2^x + I_1^y I_2^y + I_1^z I_2^z$ ), to yield

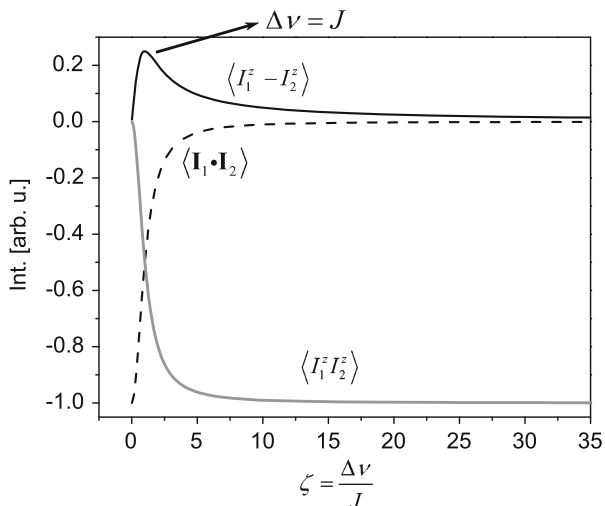
$$\rho_{(\zeta \neq 0)}^{\text{pr}}(t_f) = \mathbf{I}/4 - \eta_{\text{ZQ}_x}(\mathbf{I}_1 \cdot \mathbf{I}_2) - (1 - \eta_{\text{ZQ}_x})I_1^z I_2^z + \eta_{\text{pol}}(I_1^z - I_2^z). \quad (24)$$

In Fig. 7 the longitudinal order and the expectation values of the polarizations after the reaction are plotted vs  $\zeta$ , ranging from 0 to 35. The dotted lines represent the coefficient accompanying the term  $\mathbf{I}_1 \cdot \mathbf{I}_2$ . In the upper limit case, when  $\zeta \rightarrow \infty$ , the protons form an AX system. The terms for the coherences and polarizations are averaged out during the reaction as shown above ( $\eta_{\text{ZQ}_x} = \eta_{\text{pol}} = 0$ ), and only the longitudinal order survives.

In both limiting cases,  $\zeta = 0$  and  $\zeta \rightarrow \infty$ ,  $\langle I_1^z - I_2^z \rangle$  has a zero mean value. On the other hand, we have seen that for an AB system the latter mean value is nonzero. This suggests, assuming continuous behavior, the existence of a particular value  $\zeta^m$



**Fig. 7 PASADENA.**  
Expectation values of the longitudinal order, polarization difference and isotropic term after the reaction calculated as a function of the parameter  $\zeta = \Delta\nu/J$



for which the term  $\langle I_1^z - I_2^z \rangle$  reaches a maximum mean value. From Fig. 7 it can be seen that in fact the maximum occurs if  $\zeta^m = 1$ , i.e., if the condition  $\Delta\nu = J$  is satisfied.

### 2.6.4 Hydrogenation at Low Field and Transfer to High Magnetic Field

The plot in Fig. 7 can be interpreted not only in the sense that  $\zeta$  varies by changing the product molecule, i.e., the internal parameters, but also in a very different way. While the chemical shift difference between the two proton sites linearly depends on the external magnetic field ( $B_0$ ), the J-coupling constant is related to the chemical bond and is independent of  $B_0$  [44]. This means that the variation of  $\zeta$  can also be achieved by changing the magnetic field at which the reaction is performed. In that case, the sample must subsequently be transported from the reaction to the acquisition field. This transportation step plays an important role in the final shape of the NMR signal.

To satisfy the ALTADENA condition, for instance, the transportation must be adiabatic with respect to the internal molecular dynamics [3, 20].

### 2.6.5 Sudden vs Adiabatic Transport

In order to illustrate the effect of the transportation step on the NMR signal, we treat here two limiting cases: adiabatic and sudden magnetic field changes. These two cases were described in the frame of hyperpolarization transfer in [19, 53], and specifically related to parahydrogen in [20].

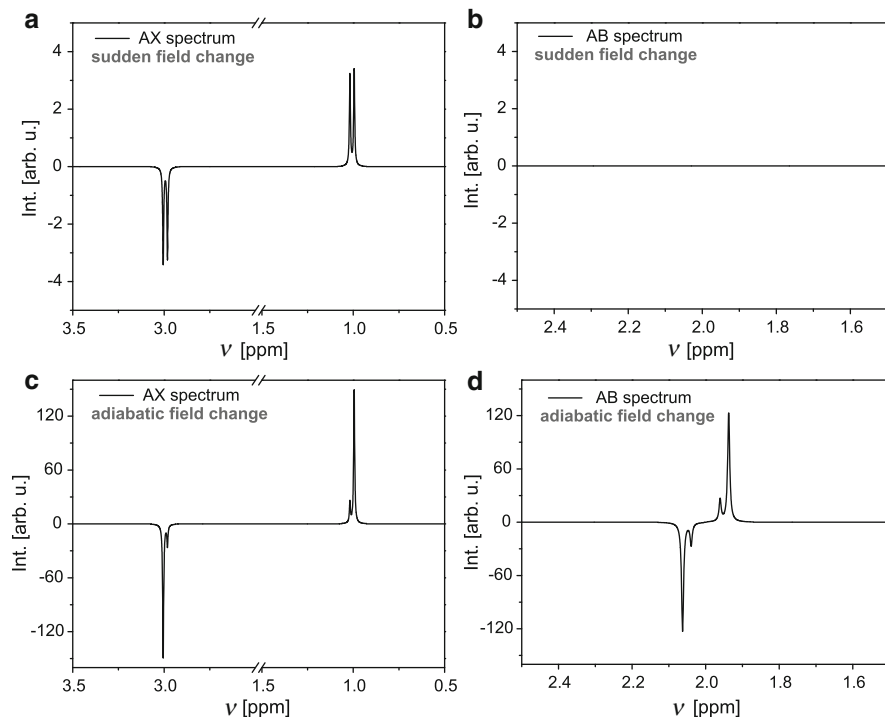


**Fig. 8** Simulated spectra obtained when the reaction is performed at low field (3 mT) and suddenly (a, b) or adiabatically (c, d) moved to the observation field (7 T). In (a, c) an AX spin system ( $\Delta\nu = 0.2$  ppm,  $J = 7$  Hz) and in (b, d) an AB spin system ( $\Delta\nu = 0.1$  ppm,  $J = 7$  Hz) were considered

For the sudden field change the transport is assumed to be *instantaneous*, in the sense that no spin evolution is allowed between the reaction and the NMR measurement. Let us assume that the reaction is performed at  $B_0 = 3$  mT and the NMR experiment at  $B_0 = 7$  T. If the protons form an AX system at high field ( $\Delta\nu = 2$  ppm,  $J_{1,2} = 7$  Hz), the averaged density operator after the reaction is  $\bar{\rho}_{\text{AX}}^{\text{PR}}(t_f) = \mathbf{I}/4 - 0.9987(I_1^x I_2^x + I_1^y I_2^y) - I_1^z I_2^z + 1.8 \times 10^{-2}(I_1^z - I_2^z)$ , or equivalently  $\bar{\rho}_{\text{AX}}^{\text{PR}}(t_f) = \mathbf{I}/4 - 0.9987(\mathbf{I}_1 \cdot \mathbf{I}_2) - 1.3 \times 10^{-3}I_1^z I_2^z + 1.8 \times 10^{-2}(I_1^z - I_2^z)$ .

At the end of the reaction almost 100% of the initial  $p$ -H<sub>2</sub> density operator is preserved. After a *sudden* transport to the observation field only the tiny terms corresponding to longitudinal order and polarization difference will contribute to the NMR spectrum (see Fig. 8a).

The spectrum's shape is dominated by  $\langle I_1^z - I_2^z \rangle$ . On the other hand, if the protons form an AB system in the product molecule ( $\Delta\nu = 0.1$  ppm,  $J_{1,2} = 7$  Hz), after the hydrogenation the initial *parahydrogen* density operator remains unchanged,  $\bar{\rho}_{\text{AB}}^{\text{PR}}(t_f) = \mathbb{I}/4 - \mathbf{I}_1 \cdot \mathbf{I}_2$ . The subsequent *sudden* transport does not affect it, and the system is NMR silent, as can be seen in Fig. 8b.

Similar calculations for both spin systems (with the hydrogenation performed again at  $B_0 = 3$  mT), but the sample *adiabatically* transported to the observation magnetic field (7 T), reveal remarkable differences in the corresponding NMR spectra.

While the averaged density operators after the reaction are exactly the same as for the sudden field change case, their evolutions with the full Hamiltonian at different magnetic field strengths transform them into  $\bar{\rho}_{\text{AX}}^{\text{pr}}(t_f) = \mathbb{I}/4 - 1.1 \times 10^{-2}(\mathbf{I}_1 \cdot \mathbf{I}_2) - 0.9885I_1^z I_2^z + 0.485(I_1^z - I_2^z)$  for the AX system and  $\bar{\rho}_{\text{AB}}^{\text{pr}}(t_f) = \mathbb{I}/4 - 0.23(\mathbf{I}_1 \cdot \mathbf{I}_2) - 0.77I_1^z I_2^z + 0.495(I_1^z - I_2^z)$  for the AB system, respectively.

The values displayed above correspond to simulations in which the sample evolved for long times at every magnetic field value from the reaction to the observation field (in 1,000 steps). The resulting spectra can be seen in Fig. 8c, d, where the differences of the *sudden* field transport are clearly manifested. The shapes of the spectra observed after adiabatic transport agree with the description given in the population approach for the ALTADENA experiment, as expected. The fact that in ALTADENA not only the reaction at low field but also the adiabaticity of the transport step is crucial to allow the coherences present in the term  $\mathbf{I}_1 \cdot \mathbf{I}_2$  to be transformed into polarization difference now becomes evident.

## 2.6.6 Different Field Variations During the Transport Step

The two limiting cases treated above serve to grasp the importance of the transport step. In practice, however, during the experiments the magnetic field change will be neither completely adiabatic nor perfectly sudden. In general, we will have a spatial field variation between the place where the reaction is performed and the center of the NMR apparatus. Furthermore, the sample will be transported through the magnetic field profile with a certain velocity. In order to include those variables in the calculations, we note that

$$\frac{dB_0^z}{dt} = \frac{dB_0^z}{dz} \frac{dz}{dt}. \quad (25)$$

The first factor on the right-hand side of the equation is the magnetic field profile, which can be easily measured. In Fig. 9a we have included such a profile obtained in our laboratory (the data shown were interpolated). The  $z$ -component of the magnetic field falls down from 7 T to about 3 mT in  $\sim 1.4$  m. The second factor on the right-hand side of Eq. (25) represents the  $z$ -component of the sample's velocity. By controlling both terms one can obtain the time dependency of the external magnetic field change and, therefore, the time dependence of the Hamiltonian, through the chemical shift part [see Eq. (21)]. The Liouville–von Neumann equation should be solved in this case step by step, because the Hamiltonians at different times do not commute (i.e.,  $[H^{\text{pr}}(t_i), H^{\text{pr}}(t_i + \Delta t_i)] \neq 0$ ).

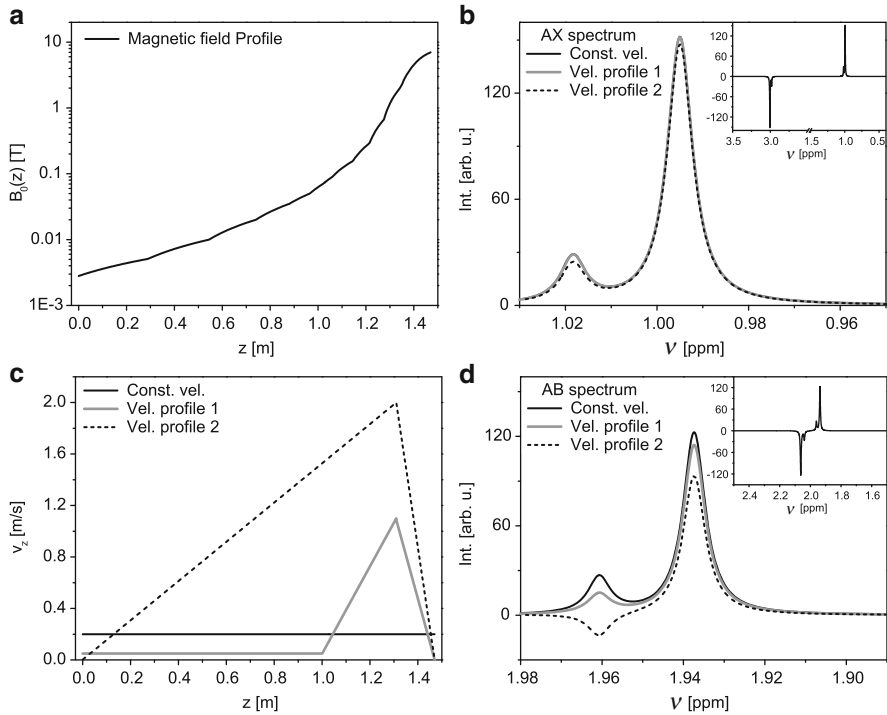


**Fig. 9** (a) Interpolated magnetic field profile in  $z$ -direction, obtained in our laboratory; (c) three different velocity profiles considered in the simulations for the sample transportation; (b) AX spectrum and (d) AB spectrum obtained for each of the velocity profiles

As an illustration, we have chosen three different velocity profiles. First, we assumed that the sample travels 1.4 m at constant velocity  $v_z = 0.2$  m/s. Second, the sample is transported at lower constant velocity,  $v_z = 0.05$  m/s for the first meter and then accelerates until being  $\sim 0.15$  m apart from the coil, followed by a deceleration until it settles at 7 T. Finally, we have considered a velocity profile which includes acceleration from the reaction place to  $\sim 0.15$  m from the magnet's center followed by a deceleration until the measurement spot. Considering these three cases we treat constant velocity, acceleration only near the top of the magnet, and acceleration in a wide field range, respectively. The three profiles can be seen in Fig. 9c.

Again, an AX and an AB spin system were introduced in the calculations and the corresponding spectra are shown in Fig. 9b, d. The spectra corresponding to the weakly coupled system seem not to be affected by variations in the velocity profile, despite some little intensity changes. On the other hand, the strongly coupled system shows a more pronounced variation in the shape of the spectra with respect to the velocity profile. Accelerating at low magnetic field values, for instance, inverts a part of the spectrum.

It can be concluded that, although visible changes in the resulting NMR spectra are observed in some cases when switching between velocity profiles, the transport step seems not to be critical for a two spin system, as the overall shape of the spectra is not grossly perturbed. However, we can anticipate more pronounced changes in larger spin systems.

### 2.6.7 Enhancement Factor

Before finishing the treatment of two spin systems we will calculate the theoretical enhancement in a PASADENA experiment for an AX spin system, using the results obtained with the density operator formalism. The enhancement is derived by considering, on one hand, the maximum signal resulting from an experiment where the hydrogenation is carried out with hydrogen in thermal equilibrium at room temperature, and, on the other hand, the maximum signal obtained from a PHIP-PASADENA experiment with enrichment factor  $\xi$ .

Assuming that the NMR experiment is carried out at temperature  $T_{\text{exp}}$ , the thermal equilibrium density operator is expressed as  $\rho^{\text{th}} = \mathbb{I}/4 - \varepsilon/4(I_1^z + I_2^z)$  [44, 46, 48]. After a  $90^\circ$  r.f. pulse, with phase  $-y$  for instance, we get  $\rho^{\text{th}} = \mathbb{I}/4 - \varepsilon/4(I_1^x + I_2^x)$ , yielding  $|\mathcal{S}_{90^\circ}^{\text{th}}| = \varepsilon/4$ .

Regarding the experiment with enriched *parahydrogen*, after the hydrogenation and before the application of the r.f. pulse, the density operator is  $\bar{\rho}^{\text{pr}}(t_f) = \mathbb{I}/4 - \xi I_1^z I_2^z$ . In contrast to the thermal equilibrium case, the maximum signal results after a  $45^\circ$  r.f. pulse [43]. The corresponding density operator just after the r.f. pulse is  $\bar{\rho}^{\text{pr}}(t_f) = \mathbb{I}/4 - (\xi/2)\{I_1^z I_2^z + I_1^x I_2^x + (I_1^x I_2^z + I_1^z I_2^x)\}$ . The NMR signal intensity is initially zero because none of the terms involved in the density operator are directly observable. However, the term  $(I_1^x I_2^z + I_1^z I_2^x)$  becomes observable after evolving with the J-coupling Hamiltonian, giving  $|\mathcal{S}_{45^\circ}^{\text{PHIP}}| = \xi/4$ . Here, we have supposed that the spectrum's line width is much smaller than the J-coupling constant.

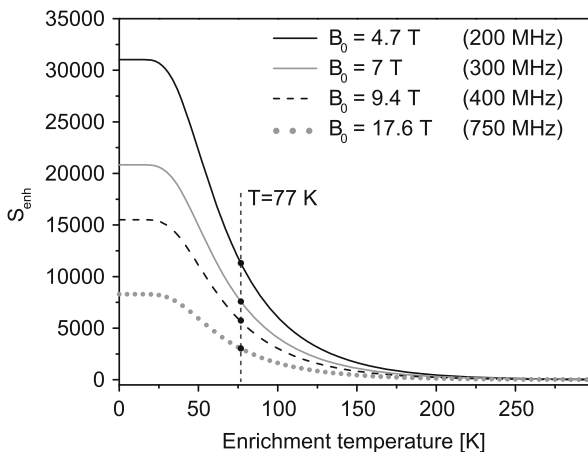
Combining both expressions, the signal enhancement as a function of the *parahydrogen* fraction is

$$S_{\text{enh}}(N_{\text{para}}) = \frac{\xi}{\varepsilon} = \frac{(4N_{\text{para}} - 1)kT_{\text{exp}}}{3\gamma\hbar B_0}. \quad (26)$$

Invoking Eq. (9), and after some algebraic manipulation, we can recast the signal enhancement as function of the temperature at which the *parahydrogen* is enriched, as

$$S_{\text{enh}}(T) = \frac{3 \sum_{J=0} (2J+1) e^{J(J+1)\theta_r/T}}{Z(3\gamma\hbar B_0/kT_{\text{exp}})}. \quad (27)$$

**Fig. 10** Enhancement factor for different observation fields  $B_0$  at room temperature, as a function of the  $p$ -H<sub>2</sub> enrichment temperature. Note that the predicted enhancement is larger for lower  $B_0$  fields



In Fig. 10 the signal enhancement is plotted for different magnetic field strengths  $B_0$  at which the PASADENA experiment is performed, setting  $T_{\text{exp}} = 300$  K. Note that the enhancement is larger for smaller magnetic fields. Remarkably, the liquid nitrogen boiling temperature falls close to the point where  $|dS_{\text{enh}}/dT|$  is maximum.

At this point it must be emphasized that the enhancement shown above is the maximum enhancement theoretically achievable. In practice, however, lower (and even much lower) values are observed associated with relaxation effects and partial peak cancellation due to the magnetic field inhomogeneity across the sample (NMR line width).

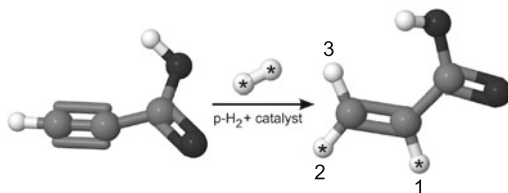
## 2.7 Larger Spin Systems and Hyperpolarization Transfer

If the former *parahydrogen* protons are deposited into sites exhibiting nonzero interaction with the rest of the product molecule (or parts of the molecule), a new issue might appear: the hyperpolarization can be partially transferred to other involved nuclei, depending on the Hamiltonian  $H^{\text{pr}}$  [14, 20, 49].

During a PASADENA experiment, the hyperpolarization might or might not be transferred from one of the former *parahydrogen* protons to a third nucleus, depending on the coupling network. If the third nucleus, labeled as  $k$ , is strongly coupled to at least one of the *parahydrogen* protons, the transfer will occur. In contrast, if the third nucleus is weakly coupled to both *parahydrogen* protons the hyperpolarization will remain confined to the  $p$ -H<sub>2</sub> sites [14].

By lowering the magnetic field at which the reaction is carried out, the weakly coupled spins can become strongly coupled and then allow the hyperpolarization to be redistributed. At *very low* magnetic field values, all spins are strongly coupled, even to heteronuclei. In this case, the hyperpolarization will spread over the whole molecule [43, 49].

**Fig. 11** Scheme of the hydrogenation of propiolic acid with *p*-H<sub>2</sub>. The former *p*-H<sub>2</sub> protons are marked with asterisks in the product molecule



We will concentrate here on a particular three spin system, the hydrogenation of propiolic acid with *parahydrogen* (see Fig. 11), to illustrate the major features of PASADENA and ALTADENA experiments. The choice of the system fulfills two purposes: first, it represents an interesting three-spin system, with a particularly large coupling between the third proton and one of the *parahydrogen* protons; second, as ALTADENA experiments on this system were already reported [26] and a set of theoretical spectra were published recently [20], it appears as a suitable well known system to be used as an example. The molecular parameters are:  $\nu_1 = 6.0$ ,  $\nu_2 = 5.8$ , and  $\nu_3 = 6.25$  ppm;  $J_{1,2} = 10.2$ ,  $J_{1,3} = 17.2$ , and  $J_{2,3} = 1.8$  Hz, respectively (data extracted from [20]).

### 2.7.1 PASADENA in a Three Spin System

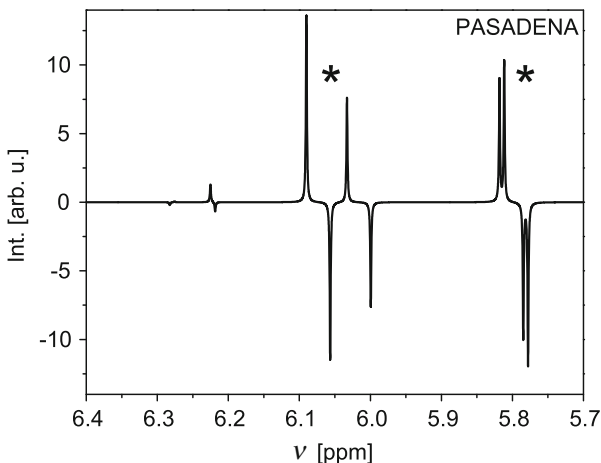
At 300 MHz Larmor frequency, the protons labeled as 1 and 2 (stemming from *parahydrogen*) are relatively strongly coupled, with  $\zeta_{1,2} \sim 6$ , as well as the protons labeled as 1 and 3, with  $\zeta_{1,3} \sim 4.5$ . In contrast, the protons labeled as 2 and 3 are weakly coupled, with  $\zeta_{2,3} \sim 75$ . Therefore, one would expect a considerable amount of hyperpolarization to be transferred to the third proton. However, the dynamics are dominated by the spins 1 and 2, and the hyperpolarization mostly remains on the former *parahydrogen* protons, at this Larmor frequency. This can be observed from the simulation shown in Fig. 12, where the peaks of the former *p*-H<sub>2</sub> protons are marked with asterisks. Although a tiny amount of polarization is observed at the site of spin 3, the calculation shows that more than 95% of the initial polarization is still at the sites 1 and 2 after the hydrogenation (of the form  $I_1^z I_2^z$ ).

### 2.7.2 ALTADENA in a Three Spin System

A very different result is obtained with the same spin system in an ALTADENA experiment. Carrying out the hydrogenation at, for instance,  $B_0 = 3$  mT, the chemical shift to J-coupling ratios are:  $\zeta_{1,2} \sim 2.5 \times 10^{-3}$ ,  $\zeta_{1,3} \sim 1.9 \times 10^{-3}$ , and  $\zeta_{2,3} \sim 3.2 \times 10^{-2}$ , respectively. Starting with  $\rho^{\text{pr}}(0) = \mathbb{I}/4 - \mathbf{I}_1 \cdot \mathbf{I}_2$ , the following averaged density operator results after the reaction:

$$\bar{\rho}^{\text{pr}}(t_f) = \mathbb{I}/4 - 0.335(\mathbf{I}_1 \cdot \mathbf{I}_2) - 0.363(\mathbf{I}_1 \cdot \mathbf{I}_3) - 0.302(\mathbf{I}_2 \cdot \mathbf{I}_3). \quad (28)$$

**Fig. 12** Spectrum simulated for the three spin system under PASADENA conditions. The marked peaks refer to the former  $p$ -H<sub>2</sub> protons. The third proton is not influenced by the hyperpolarization



The initial hyperpolarization is almost equally distributed in the three spin system. The expectation values are directly related to the ratios of  $\zeta$ . If the averaged density operator is expressed as  $\bar{\rho}^{\text{pr}}(t_f) = \mathbb{I}/4 - \sum_i c_{i,j} \mathbf{I}_i \cdot \mathbf{I}_j$  (with  $\sum_i c_{i,j} = 1$ ), it is observed that  $c_{1,3} > c_{1,2} > c_{2,3}$  when  $\zeta_{1,3} < \zeta_{1,2} < \zeta_{2,3}$ . This means the stronger the coupling the larger the hyperpolarization fraction obtained.

The hyperpolarization distribution can be directly seen in the plot in Fig. 13a. The NMR spectrum (45° r.f. pulse) acquired in a 7-T magnet after an adiabatic sample transportation, i.e., the typical ALTADENA experiment, is shown in Fig. 13b.

Despite the hyperpolarization transfer, which is almost absent in PASADENA experiments, there is another remarkable difference between ALTADENA and PASADENA spectra: while the signals in PASADENA are in antiphase, the adiabatic sample transport to the acquisition magnetic field in ALTADENA produces net polarization in the spins 2 and 3, keeping the antiphase character only on spin 1. If the transport step is modified, however, the overall shape of the spectrum is strongly affected. The five spectra in Fig. 14 show the differences when varying the way in which the sample is transported to the magnet from the same reaction field. The labels correspond to the velocity profiles introduced in Fig. 9. Moving the sample constantly at 0.05 m/s seems not to affect the adiabaticity of the transport, while doing it at 0.2 m/s nearly destroys the signal, as expected in the case of a sudden transport (see Fig. 8). On the other hand, accelerating the sample either from the reaction field or only from relatively high field produces a great discrepancy with the adiabatic case.

The results described in this section can generally be extended to cases when the protons originating from *parahydrogen* are deposited into sites coupled to larger spin systems. The most striking difference will appear in ALTADENA experiments where, depending on the reaction field, the hyperpolarization might migrate even to heteronuclei. At the Earth's magnetic field or lower, for example, hyperpolarization transfer to <sup>13</sup>C is very well feasible [14, 50, 54].



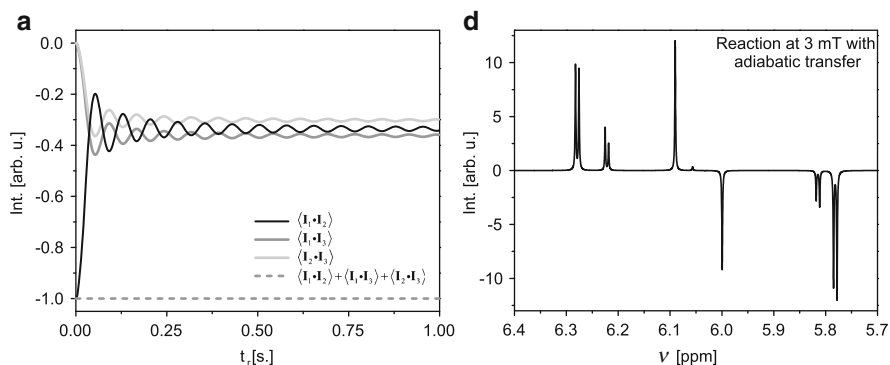


**Fig. 13** Three spin system under ALTADENA conditions. (a) Expectation values of the isotropic operators during the chemical reaction at 3 mT magnetic field strength; (b) simulated NMR spectrum after an adiabatic transport to 7 T magnetic field strength

### 3 Experimental Results and Applications

In this section, two practical applications and experiments using *parahydrogen* Induced Polarization employing homogeneous catalysis to enhance NMR signals are presented. There are numerous fields where nuclear magnetic resonance (NMR) has nowadays proved to be essential. However, the poor NMR signal has always been a drawback which can be overcome by means of PHIP [55]. The first application presented in this chapter shows the capability of using PHIP in  $^1\text{H}$  magnetic resonance imaging (MRI) where not only the enhanced signal can be exploited to generate MRI contrast but also the difference in the initial spin state of the PHIP polarized protons compared to the thermal polarization of the background. The second application chosen for this chapter shows a method to provide the enhanced hyperpolarized signal in a continuous fashion, making it possible to perform traditional 2D NMR experiments much faster.

In this chapter, two different substrates are used as model compounds for the hydrogenation with *p*- $\text{H}_2$ . Both of them show an excellent acceptance of the *p*- $\text{H}_2$  molecule. The model compounds are chosen because of their different properties: one is soluble in water and the other one in acetone, thus providing examples for experiments in aqueous and organic systems. As explained in the preceding section, the experiments shown here correspond to a homogeneous reaction with enriched *p*- $\text{H}_2$ , which enables a pairwise transfer of the *p*- $\text{H}_2$  protons to the substrate.

#### 3.1 Catalytic Systems

The catalytic systems presented here for PHIP are homogeneous catalyst complexes with rhodium as metal center. They are cationic in order to prevent isomerization as a side reaction. Unfortunately, most commercially available homogeneous catalysts

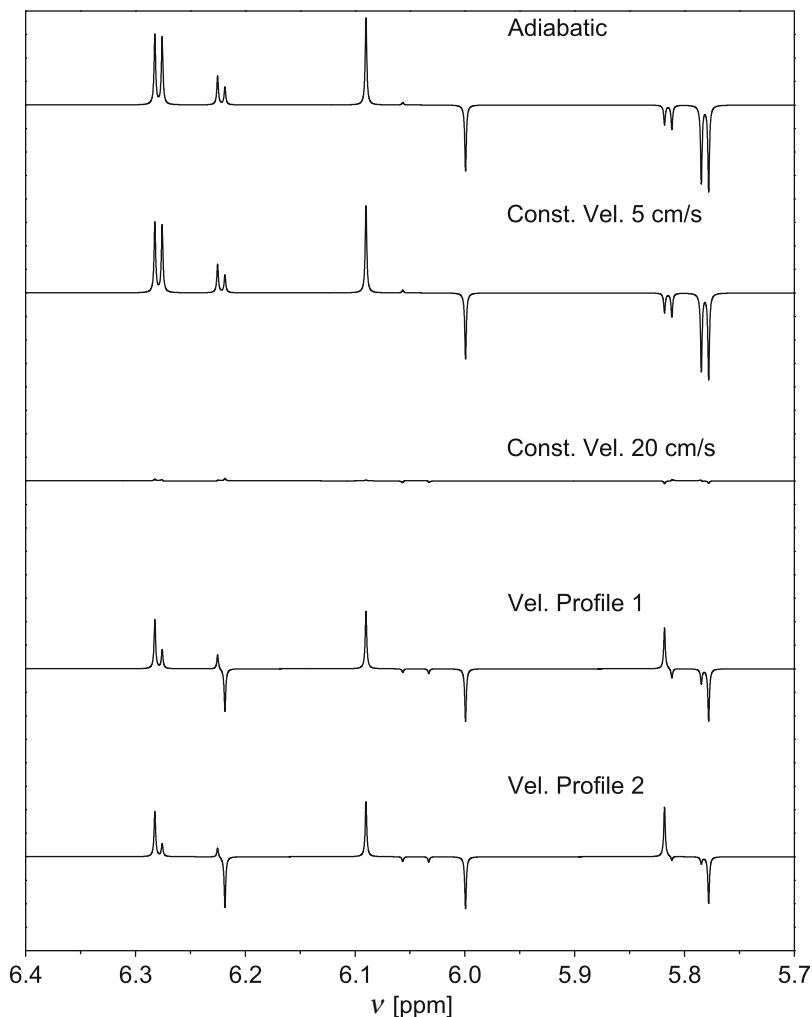


**Fig. 14** Hydrogenation of propiolic acid: simulated spectra were obtained by using different velocity profiles during the transportation to high magnetic field

are soluble only in organic solvents like acetone or methanol, not in water. This is the case for the catalyst shown in Fig. 15a.

To date, water-soluble PHIP catalysts are not commercially available, but the most popular one can be easily synthesized [56]. In order to enhance the solubility in aqueous solvents, polar groups, e.g., sulfonate groups, are added to the ligand system of the catalyst. One drawback of this intervention into the electron density of the ligand system is the possible deactivation of the total catalyst. Fortunately, this is not always the case and, in Fig. 15b a water-soluble catalyst is shown whose capability to enable the pairwise transfer of the protons to the substrate had been proved [56].

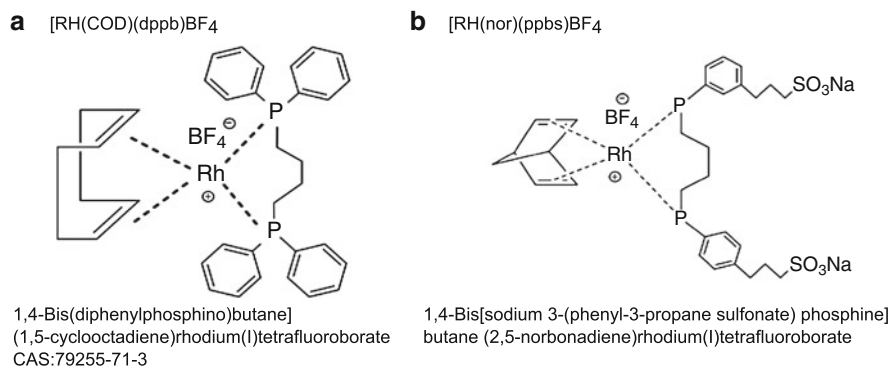


**Fig. 15** Homogeneous PHIP catalysts: (a) water insoluble catalyst; (b) water soluble catalyst

Both catalyst systems presented here have shown a high activity and low substrate specificity; moreover they ensure the pairwise transfer of  $\text{H}_2$  to the substrate molecule. The embedding of stereo information is possible. Unfortunately, the most important disadvantage of them is that both are toxic and they must be removed if a medical application is considered [57].

## 3.2 The Model Compounds

As mentioned above, two model compounds are used in the presented experiments. Whenever possible, the experiments are shown in both compounds in order to allow for a comparison: 1-hexyne is used for reactions in organic solvents and 2-hydroxyethylacrylate for reactions under aqueous conditions.

### 3.2.1 1-Hexyne

1-Hexyne is a highly flammable liquid, with a boiling point between  $71^\circ\text{C}$  and  $72^\circ\text{C}$ , and it is commercially available. As can be seen in Fig. 16, hydrogenation of the terminal triple bond results in 1-hexene.

1-Hexyne is barely sterically hindered, which makes it a good model compound allowing excellent interaction to several catalysts. The hyperpolarized double bond shows a long spin-lattice relaxation time  $T_1$  of approximately 30 s, whereas the relaxation times of all other protons in the molecule are around 15 s.

### 3.2.2 2-Hydroxyethyl Acrylate

2-Hydroxyethyl acrylate is the water soluble model compound used in the experiments. It is a toxic liquid having its boiling point between  $210^\circ\text{C}$  and

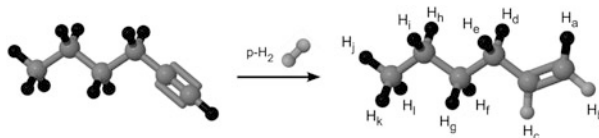
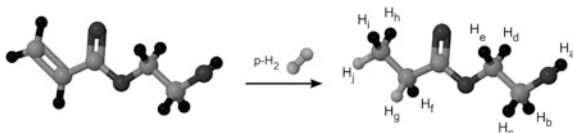


**Fig. 16** Hydrogenation of 1-hexyne leads to 1-hexene

**Fig. 17** Hydrogenation of 2-hydroxyethyl acrylate leads to 2-hydroxyethyl propionate



215°C, and it is also commercially available. In Fig. 17 the hydrogenation of 2-hydroxyethyl acrylate is shown, resulting in the reaction product 2-hydroxyethyl propionate. The  $T_1$  relaxation time of the hyperpolarized protons is approx. 5 s, which is substantially shorter than the one of 1-hexene.

### 3.3 *PHIP Hyperpolarized Substances as Contrast Agents in $^1\text{H}$ MRI*

Magnetic Resonance Imaging (MRI) is one of the most interesting targets for PHIP applications. So far, medical imaging with hyperpolarized compounds was realized with  $^{13}\text{C}$  or  $^{15}\text{N}$  hyperpolarized substances, which have the advantage of negligible background signal, very long  $T_1$  times, and large chemical shift ranges [58].

Very exciting medical applications of substances with hyperpolarized heteronuclei have already been demonstrated like tumor diagnosis [59–61] or in vivo pH mapping [62]. However, MRI of heteronuclei is technically demanding and thus expensive, because it requires the use of additional hardware (e.g., broadband amplifiers and coils). Moreover, co-registration with a high-resolution proton image is necessary to obtain anatomical information. Thus, using the standard NMR and MRI nucleus—the proton—for molecular imaging would be beneficial. However, the huge amount of protons present in the body gives rise to an NMR signal far exceeding that of a small amount of hyperpolarized protons. As a consequence the hyperpolarized signal is difficult to distinguish from the thermal background. In addition, the antiphase character of the PHIP signal can produce signal cancellation, making the desired contrast even more difficult to achieve. However, there is a simple method recently proposed [15] which manages to take advantage of the special PHIP spin state, thus enabling the use of PHIP hyperpolarized compounds as contrast agents in  $^1\text{H}$  MRI. Because of its practical interest and novelty this was chosen to be the first application presented in this chapter.

The idea exploits the differences between the initial spin state of the  $p\text{-H}_2$  and the thermally polarized protons (see the theoretical section). The procedure was applied to both model compounds introduced above. In both cases good contrast was observed, manifesting the general validity of the proposed method. Below, the method is introduced and each experiment is preceded by a short theoretical description of the main concepts involved. As the theoretical descriptions are intended to be only pictorial, some helpful assumptions are made:

1. For the PHIP compound an AX spin system is assumed, even though the real systems are more complicated (see Figs. 16 and 17) and, as explained in the theoretical section, more than two spins should be used when performing exact calculations. However, the main features of the PHIP signal observed here can be explained using this simplification.
2. The thermally polarized molecules of the background, i.e., the system from which the PHIP signal should be distinguished, possess a single resonance line (for example water).
3. The pulses of the NMR sequence are set on-resonance with the thermal background.

All experiments treated here were performed under PASADENA conditions (although the contrast works also for ALTADENA) using a clinical 1.5-T MRI system (Magnetom Sonata, Siemens Medical, Erlangen, Germany) and a basic FLASH imaging pulse sequence with centric reordering.

There are several cases regarding the spatial confinement of the hyperpolarized substance we should distinguish when discussing these experiments. These different cases depend not only on the  $T_2^*$  decay times of each component but also on the relative signal amplitude differences. According to the relative  $T_2^*$  relationship the following two cases should be separately analyzed.

### 3.3.1 Case 1: Thermal Signal Decays Faster than Hyperpolarized Signal

Let us first consider the case where the decay of the thermal signal of the background molecules is faster than the decay of the hyperpolarized signal. Experimentally this condition can be achieved by confining the hyperpolarized molecules to a small volume placed in the middle of the magnet and by surrounding them with a large volume of thermally polarized molecules. As the magnetic field is more homogeneous close to the center of the magnet,  $T_2^*$  in this region should be longer than in the outer part. In Fig. 18 the phantom used for this experiment is shown together with a representation of the FIDs corresponding to the AX system (Fig. 18a) and the experimentally data obtained with 1-hexene (Fig. 18b).

In a PASADENA experiment, the initial state of an AX spin system is  $\bar{\rho}^{\text{PF}}(t_f) = \mathbb{I}/4 - \xi I_1^z I_2^z$ , as theoretically explained in the first section, and after application of a  $45^\circ$  pulse it is converted into an oscillating observable signal of the form

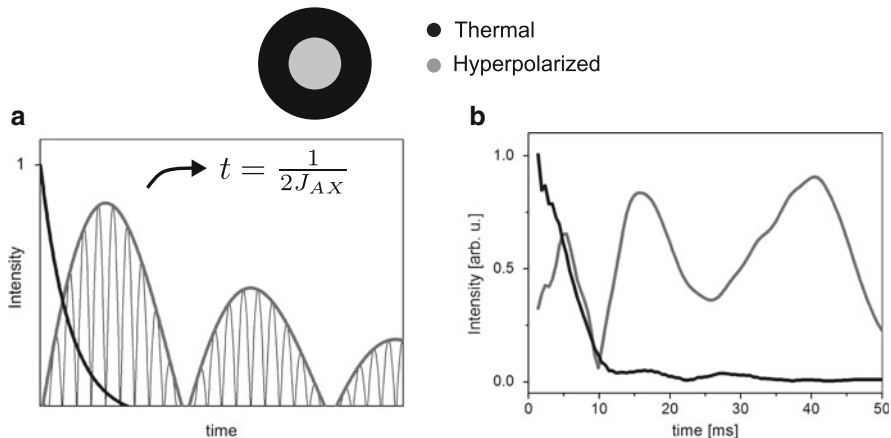


**Fig. 18** Experimental configuration for case 1 where the hyperpolarized compound is confined to a small area. **(a)** Calculated fast decaying thermal signal (*black line*) compared to the oscillating hyperpolarized signal (*gray line*). **(b)** Experimental data for water and 1-hexene

$$\rho^{45^\circ \rightarrow y}(t) = \mathbb{I}/4 - \xi \sin(\pi J_{AX}t)(I_1^y + I_2^y). \quad (29)$$

From this equation it can be shown that the maximum signal of the hyperpolarized compound occurs at  $t = (2J_{AX})^{-1}$ , as indicated in Fig. 18a. The possibility of exploiting this oscillatory behavior to generate the desired contrast can be understood from the figure: at the time when the amplitude of the hyperpolarized signal is maximal, the thermal signal is almost negligible. In Fig. 18b the experimental data obtained for a phantom with hyperpolarized 1-hexene in the inner tube and water in the outer tube are shown. Even though 1-hexene is a large spin system as shown in Fig. 16, the oscillatory behavior of the two  $p$ - $H_2$  protons dominates the FID and the position of the maximum signal ( $\approx 16$  ms) can easily be determined.

Once the position of this maximum difference between both signals is known this time can be set as the echo time  $T_E$  in the imaging sequences to highlight the difference, i.e., maximize the contrast. In Fig. 19, images obtained for eight different echo times ( $T_E$ ) in the imaging pulse sequence are shown for the two model compounds. The oscillation of the signal amplitude of the inner tube can be clearly recognized for both hyperpolarized substances, whereas the signal of the outer tube, containing water, decays with increasing echo time. As predicted, the best contrast is observed when the echo time corresponds to the maximum of the hyperpolarized signal (for 1-hexene  $T_E \sim 16$  ms and for 2-hydroxyethyl propionate  $T_E \sim 15$  ms). Of course, the spin systems of the two hyperpolarized components are different but both show the J-coupling induced refocusing of the signal as theoretically predicted when starting from a PASADENA experiment. This demonstrates that the method can easily be applied to different molecules which can be hyperpolarized via PHIP and highlights its general applicability.

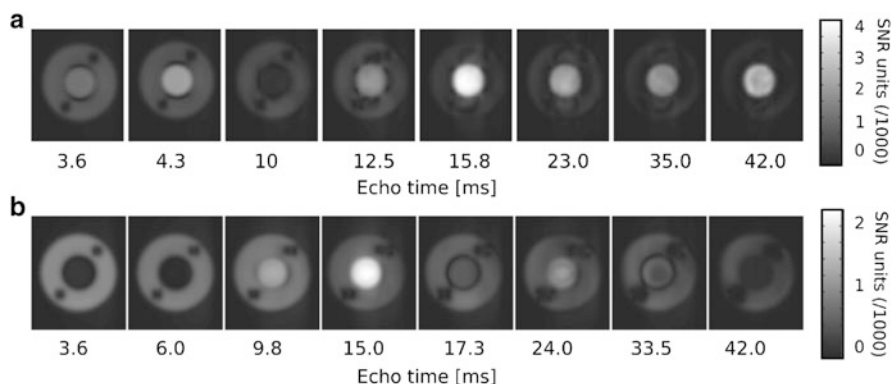


**Fig. 19** Images acquired with different echo times ( $T_E$ ) in the MRI pulse sequence, for 1-hexene (*top*) and 2-hydroxyethyl propionate (*bottom*)

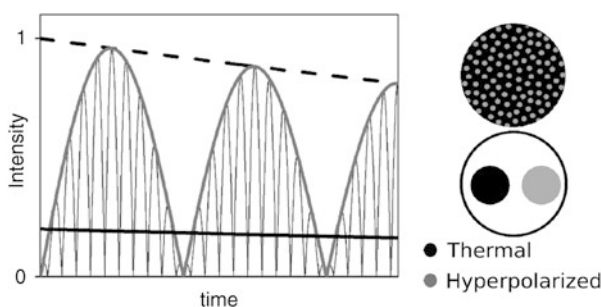


**Fig. 20** Identical  $T_2^*$  decays for the hyperpolarized and the thermally polarized substance. Two different signal amplitudes for the thermal signal are plotted (*straight and dotted lines*)

### 3.3.2 Case 2: Similar or Identical Decay Times

Another interesting case occurs when the hyperpolarized and the thermal signal both decay with the same  $T_2^*$  time constant. In Fig. 20 the theoretical representations of the FID signals are schematized for this case. The experimental set up can be either two tubes at the same position relative to the center of the magnet or a mixture of both (thermally polarized and hyperpolarized) compounds contained in the same tube.

In Fig. 20 two possible scenarios for the amplitude of the thermal signal are plotted. The dotted line corresponds to the case where the amplitude of the thermal signal is comparable to the amplitude of the hyperpolarized signal. The solid line resembles the case where the hyperpolarized signal is noticeably larger than the thermal signal.

In the latter case we can once more obtain a good MRI contrast by choosing the optimal echo time for the hyperpolarized substance as can be concluded from the experimental data representing this case shown in Fig. 21.

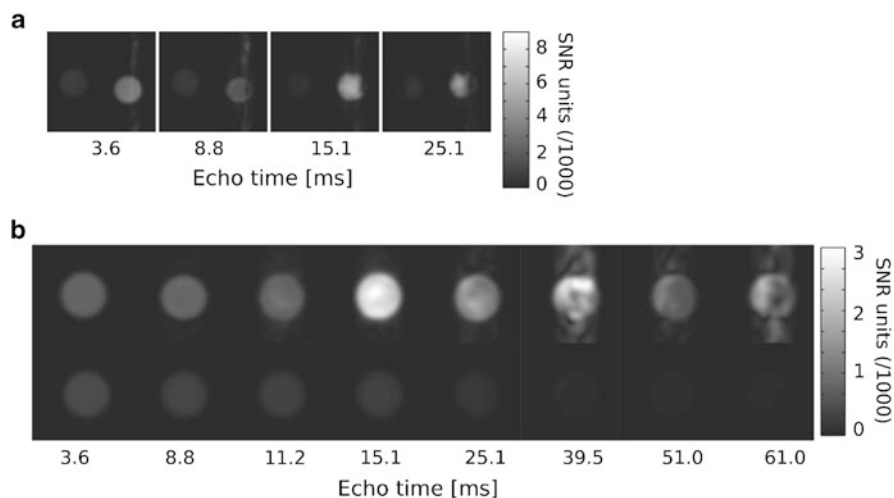


**Fig. 21** (a) The left tube contains water and the right one hyperpolarized 1-hexene. (b) One single tube contains hyperpolarized 1-hexene dissolved in a non-deuterated solvent. For both phantom geometries the best contrast is observed for 15 ms echo time

The phantom consisting of two tubes contained water and hyperpolarized 1-hexene, whereas the experiments with only one tube (containing both the hyperpolarized fluid and the thermally polarized background molecules) were performed with 1-hexene dissolved in non-deuterated acetone. The spin density of the proton background is somewhat smaller in this case, as for the pure water phantom, but still much higher than the spin density of the hyperpolarized protons. Because 1-hexene can be hyperpolarized very efficiently by using PHIP it is nonetheless easy to fulfill the condition that the hyperpolarized signal is exceeding the thermal one. The experiments in Fig. 21 show once more the good contrast that can be obtained for the echo time agreeing with the position of the maximal hyperpolarized signal,  $T_E = 15$  ms, for both phantom geometries.

In the less preferable case, where both signal amplitudes are identical, it is not possible to generate a contrast by using an echo time which corresponds to the maximum of the hyperpolarized signal. Certainly it is still possible to obtain a negative contrast if the chosen echo time corresponds to a minimum of the hyperpolarized signal. In this case the hyperpolarized signal cannot be observed and its location appears dark in the images.

However, a negative contrast is not optimal because dark regions in MRI images can have many causes (e.g., susceptibility differences, etc.). Therefore we developed a method to obtain a positive contrast even in this case, which is explained in the following.



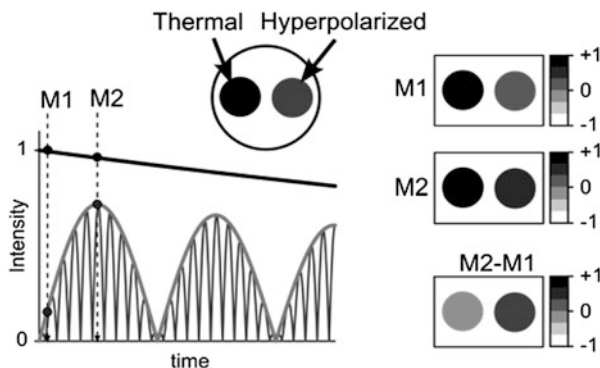


Fig. 22 Two images with different echo times are subtracted to generate the desired contrast

### 3.3.3 Contrast by Subtraction Method

The method requires the acquisition of two images with different echo times and is schematized in Fig. 22. The echo times should be chosen such that for the first echo time the signal of the thermally polarized background is maximal whereas the contribution of the hyperpolarized substance is almost zero and for the second echo time the hyperpolarized signal should be maximal while the thermal signal remains almost unaltered. These echo times are labeled as M1 and M2 in Fig. 22. Subtraction of these images results in a new image where the hyperpolarized signal is positive in contrast to the signal of the thermally polarized background which is always negative due to its decay with  $T_2^*$ . This allows for an unambiguous differentiation of the two areas by sign.

In Fig. 23 the subtraction method is applied for the two model compounds studied in this section. In both cases an excellent contrast is obtained and the differentiation of the two areas by signal sign could be verified. This method would allow for a substantial reduction of the concentration of the hyperpolarized component in the experiments. It reaches its limits when the signal of the hyperpolarized component becomes comparable to the noise level of the images.

In this section we introduced a novel MRI contrast which allows for the discrimination of a small amount of PHIP hyperpolarized protons from a huge amount of surrounding thermally polarized protons. The contrast arises from the different time evolution of the PHIP hyperpolarized proton signal compared to the evolution of the normal (thermally polarized) proton signal and can be simply implemented by using basic product pulse sequences (FLASH, TrueFISP, EPI), which are varied in a minor way by only choosing the optimal echo time for the hyperpolarized substance. The optimal echo times can simply be found by recording an FID of the hyperpolarized substance prior to image acquisition.

The new method might be applied for metabolic imaging, perfusion MRI, or catheter visualization during MRI guided interventions using only conventional proton pulse sequences and equipment (NMR coils), which reduces the technical

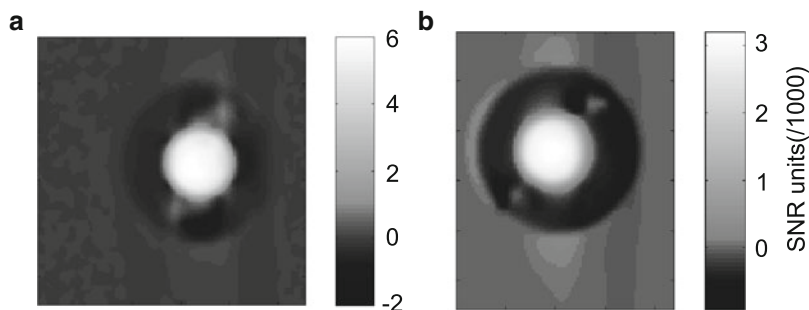


**Fig. 23** Subtraction images of images acquired with different echo times for (a) 1-hexene and (b) 2-hydroxyethyl propionate

demands that arise from MRI of heteronuclei. Moreover, Most heteronuclei (especially  $^{13}\text{C}$  and  $^{15}\text{N}$ ) have a low gyromagnetic ratio, which makes it difficult to provide images with very high spatial resolution because the gradient strengths of conventional MRI systems is limited and usually optimized for protons. Our method can be used not only for our model substances but for every molecule which can be hyperpolarized via *parahydrogen* Induced Polarization, which includes a large number of biological relevant molecules, e.g., succinate [63] (component of the citrate cycle) or barbiturates [64] (anesthetics). This variability concerning molecules and different clinical applications in combination with the simplicity of our method may result in widespread usage in MRI.

### 3.4 *Continuous Generation of a Hyperpolarized Fluid Using PHIP and Hollow Fiber Membranes*

Despite the many important applications hyperpolarization techniques have found in natural sciences and medicine, several general problems remain. The most severe limitation is the limited lifetime of the hyperpolarized state caused by  $T_1$  relaxation. This problem is less pronounced for hyperpolarized noble gases ( $^{129}\text{Xe}$ ,  $^3\text{He}$ ) which exhibit  $T_1$  times of hours [65]. In liquids efficient relaxation processes restrict the hyperpolarization to last typically from seconds to, at best, a few minutes. Fortunately, this drawback can be at least partially overcome by storing the fast decaying hyperpolarization in slowly relaxing singlet states [22, 23, 28, 66, 67]. Another shortcoming is the partial destruction of the hyperpolarization by the application of r.f.-pulses, rendering the usage of complex pulse sequences for multi-dimensional NMR experiments difficult. This can be circumvented via stepwise use of the generated hyperpolarization by applying only small flip angles [68] or by using specially designed sampling strategies [69, 70]. Another very intriguing concept to avoid these severe limitations is to use the hyperpolarization methods in a continuous flow fashion providing a continuous supply of hyperpolarized molecules or atoms.

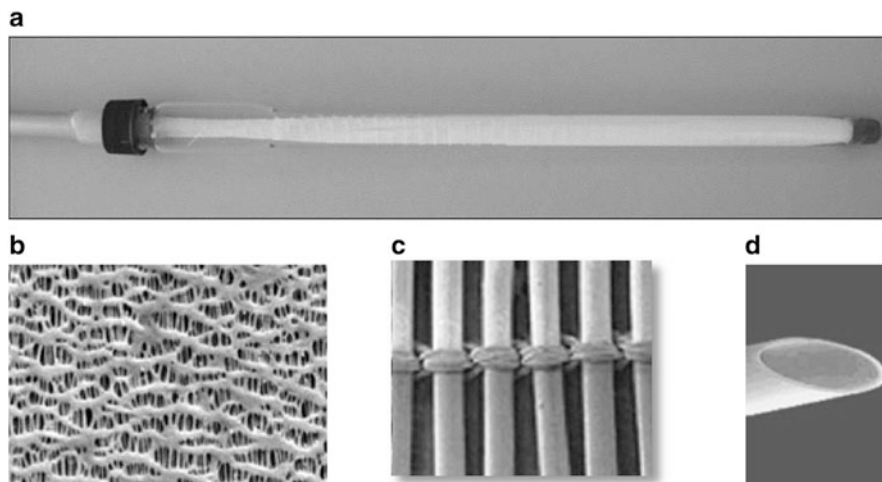


**Fig. 24** (a) Hollow fiber membranes implemented in an NMR tube; (b–d) different magnifications of the membrane fibers

In the following section a very efficient method to generate continuously a hyperpolarized fluid via PHIP using hollow fiber membranes is presented. The technique employs commercially available hollow fiber membranes for the dissolution of the  $p\text{-H}_2$  gas in the liquid sample [71]. The idea was originally developed for the dissolution of hyperpolarized  $^{129}\text{Xe}$  into liquids and was introduced in 2006 under the name XENONIZER [72, 73]. The microfibers of the membranes are thin-walled, opaque, and made from polypropylene (see Fig. 24).

Polypropylene is a hydrophobic polymer and therefore a polar solvent is unable to pass through the membrane walls. By implementing hollow fiber membranes into an NMR tube containing the PHIP precursor and catalyst dissolved in a polar solvent (e.g., water) and connecting the membranes to a reservoir of  $p\text{-H}_2$  gas, hyperpolarization of the sample can be achieved over a long time until all precursor molecules are consumed. This continuously generated hyperpolarization can easily be used either for averaging (to obtain a high SNR in very diluted samples) or to perform 2D experiments. The membranes exhibit very large gas–liquid interfaces, providing the opportunity to bring gas molecularly into solution, thereby preventing the formation of bubbles and foam. Therefore a high spectral resolution can be maintained with the membrane setup while the  $p\text{-H}_2$  gas is continuously delivered to the sample. This is normally a problem when the gas is introduced into the sample by bubbling where strong susceptibility artifacts occur. Because of this absence of foaming and bubbles, it is not necessary to stop the gas flow in the membrane experiments and wait before the measurement, thus avoiding unnecessary  $T_1$  relaxation of the sample.

It was proved that the dissolution of the gas into the solvent via the membranes happens on a time scale of milliseconds and also that the amount of dissolved gas

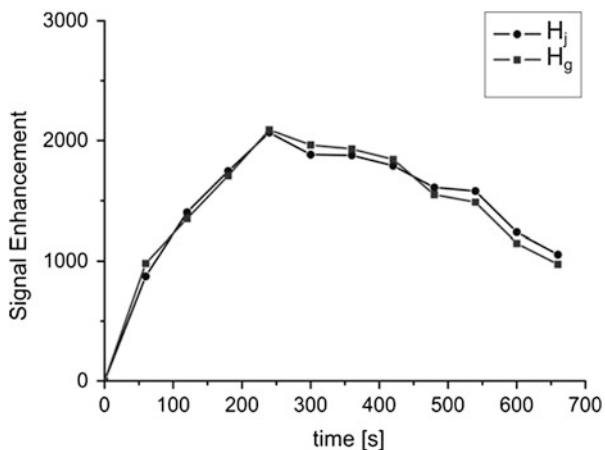


**Fig. 25** Time evolution of the signal enhancement of the hyperpolarized protons

comes close to the theoretical Ostwald solubility [72]. It is, however, important to mention a drawback of the membrane setup: it can only be used in aqueous solutions. This fact limits the possibility of using the membranes in all PHIP applications since the majority of PHIP catalysts are not soluble in water.

We present below the hydrogenation of the model compound 2-hydroxyethyl acrylate (Fig. 17) by continuously dissolving  $p$ -H<sub>2</sub> in an aqueous solution employing such hollow fiber membranes under PASADENA conditions. To enhance the conversion of the PHIP reaction the experiments are performed at 80°C. The generated hyperpolarized product shows an anti-phase spectrum free of artifacts. In Fig. 25 the signal amplitude of the hyperpolarized protons is plotted as a function of time.

At the beginning of the experiment, a build-up of the hyperpolarized signal can be observed, due to the increasing conversion of the hydrogenation reaction after the  $p$ -H<sub>2</sub> flow is switched on. In the course of the reaction the intensity of the hyperpolarized signal decreases owing to lower amounts of starting material. However, during a time of approximately 7 min (much longer than the spin-lattice relaxation of the hyperpolarized protons of ~5 s) the achieved hyperpolarized signal remains almost constant.

### 3.4.1 PHIP <sup>1</sup>H-<sup>1</sup>H COSY

As an example of the possibilities arising when the hydrogenation is performed in a continuous fashion through the membranes, we present here an interesting application: the fast acquisition of a 2D NMR spectrum, namely a <sup>1</sup>H-<sup>1</sup>H COSY [74, 75] spectrum. This kind of routine experiment, which is very useful and widely employed in spectroscopic NMR, also provides a rigorous test in order to check whether or not

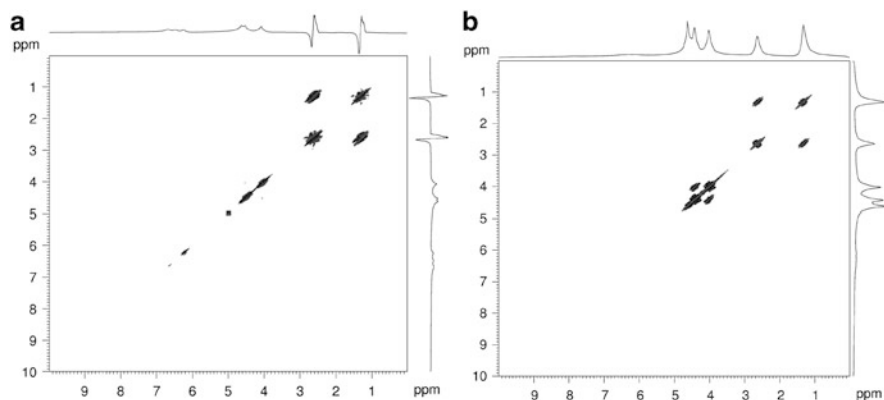


**Fig. 26** (a) PHIP  $^1\text{H}$ - $^1\text{H}$  COSY spectrum, one scan, duration: 7 min 18 s. (b) Reference  $^1\text{H}$ - $^1\text{H}$  COSY spectrum, eight scans, duration: 57 min 45 s

constant hyperpolarization is obtained with the described setup. In the presented PHIP experiments the first  $90^\circ$  pulse of the COSY sequence was replaced by a  $45^\circ$  pulse [76] to ensure an optimal excitation of the PASADENA spin state.

In Fig. 26a, the PHIP  $^1\text{H}$ - $^1\text{H}$  COSY spectrum acquired with one scan is shown; the experimental time was only 7 min 18 s. After full conversion of the hydrogenation reaction a reference experiment was performed and the thermally polarized  $^1\text{H}$ - $^1\text{H}$  COSY spectrum obtained is shown in Fig. 26b. The COSY experiment of the thermally polarized sample required eight scans and lasted 57 min 45 s. Two main differences are observed between the two 2D spectra: in the PHIP case only the cross-peaks of the hyperpolarized protons at around 1.5 and 3.0 ppm are visible due to the enhanced signal of these protons and their particular initial spin state. Additionally, the acquisition during the ongoing reaction led to the observation of small signals between 6 and 7 ppm stemming from the double bond of the starting material. These peaks are not observed in the thermal case because the latter was acquired with the fully converted sample. A small artifact (at 5 ppm) can be identified in the middle of the PHIP 2D spectrum, which arises from the lack of phase cycling in the one scan PHIP COSY experiment.

The experiments presented above show the possibility of recording a reliable 2D spectrum with chemical selectivity in a much shorter time than by measuring a sample with thermal polarization only. From the comparison between the PHIP and reference COSY experiments it can also be concluded that the enhanced signal achieved with the membrane setup remained almost constant at least for the time required for the COSY experiment.

There are many possible applications for PHIP experiments employing hollow fiber membranes. It is worth emphasizing, for example, that by using appropriated pulse sequences (like the PH-INEPT<sup>+</sup> sequence [16]) the accomplished proton polarization can be continuously transferred to heteronuclei, like  $^{13}\text{C}$ , allowing for experiments with continuously hyperpolarized heteronuclei [71]. The presented

technique opens up the possibility of investigating otherwise elusive reaction intermediates because of the possibility of accumulating several scans during the ongoing reaction. Thus, the full site selectivity provided by PHIP can be exploited. The membrane technique can easily be extended to produce a continuous flow of a hyperpolarized liquid by using a slightly different setup which we described in [72]. This method, especially when combined with an important technique recently developed by Adams et al. [77], which overcomes the restriction of the PHIP technique to unsaturated molecules, would allow for the continuous production of hyperpolarized molecules giving rise to new applications in natural sciences and medicine.

The two applications presented here are of course only examples of the many possibilities in the still open and constantly developing field of NMR and PHIP.

## 4 Conclusion

In this chapter we have presented an overview of the major features of *parahydrogen* Induced Polarization (PHIP) employing homogeneous catalysis to enhance NMR signals. An introductory theoretical approach was depicted and illustrated with two interesting applications.

First, we have explained in simple terms how hydrogen can be enriched in the *para*-state. In order to explain the NMR signal enhancement associated with PHIP experiments, two different approaches were used. The first was the well known population approach, commonly found in the PHIP literature [36]. In this context, the former *parahydrogen* protons are considered as a weakly coupled two spin system (AX) in the target molecule. The overall shape and intensity of the different PHIP spectra, i.e., PASADENA and ALTADENA, can be understood from the population differences of the two-spin energy levels. Even though this model is useful to understand the physics of PHIP in an intuitive fashion, it represents a simplification. If, for instance, the *p*-H<sub>2</sub> protons form a more strongly coupled spin system in the target molecule, such as an AB spin system, the model is no longer suitable. Moreover, if couplings to other nuclei are present, the model rapidly becomes extremely complicated. With this in mind, we have introduced a second theoretical approach in this chapter: the treatment of PHIP experiments with the density operator formalism. This method is more flexible and can be used to describe more complex spins systems, although it is mathematically more demanding. In particular, we have adopted a numerical approach here. Features such as the dependence of the shape of the spectra on the pulse duration, hyperpolarization transfer to a third nucleus, different ways to transport the sample from the hydrogenation place to the NMR apparatus, and the response to pulse sequences can be included here in a relatively simple way.

In the second part of the chapter, two examples of recent applications of PHIP are presented. The first example shows the feasibility of using PHIP hyperpolarized molecules as contrast agents in <sup>1</sup>H MRI. The method exploits the fact that thermal

in-phase and hyperpolarized anti-phase signals originate from different initial spin states and, as a consequence, evolve differently during the period between excitation and acquisition in NMR experiments. Because of this difference, a simple variation of a waiting time in the MRI sequence is sufficient to generate outstanding contrast between a small amount of hyperpolarized molecules and a large excess of thermally polarized molecules. Optimal waiting times can simply be found by recording an FID of the hyperpolarized substance prior to image acquisition. Possible applications of this method include metabolic imaging, perfusion MRI, or catheter visualization during MRI guided interventions. Additionally, it could be of considerable help in chemistry, for instance for the investigation of different reactor designs, or for the optimization of lab-on-a-chip devices like micromixers, where the flow and mixing of two components must be studied on very small length scales.

The second example shows the possibility of producing hyperpolarization with PHIP in a continuous fashion by employing hollow fiber membranes. The continuous generation of hyperpolarized samples can overcome the problem of fast relaxation times commonly involved in liquid state NMR. The use of hollow fiber membranes to dissolve molecularly *p*-H<sub>2</sub> gas in the PHIP reaction mixture in a continuous fashion enables one to generate hyperpolarization in a sample over at least some minutes. This allows for the recording of a reliable 2D spectrum much faster than when performing the same experiment with thermally polarized protons. Furthermore, the described membrane setup opens up new possibilities in the field of reaction intermediates research because of the feasibility of accumulating several scans during the reaction. The membrane technique can be easily extended to produce a continuous flow of a hyperpolarized liquid for MRI, with direct applications in chemistry, biology, or medicine.

**Acknowledgments** The authors gratefully acknowledge financial support by the Max Planck Society, the German research foundation (DFG, FOR474), and the Federal Ministry of Education and Research (VIP0199). We thank Membrana GmbH for provision of the hollow fiber membranes.

## References

1. Bowers CR, Weitekamp DP (1987) *J Am Chem Soc* 109(18):5541–5542
2. Eisenschmid TC, Kirss RU, Deutsch PP, Hommeltoft SI, Eisenberg R, Bargon J, Lawler RG, Balch AL (1987) *J Am Chem Soc* 109(26):8089–8091
3. Pravica MG, Weitekamp DP (1988) *Chem Phys Lett* 145(4):255–258
4. Natterer J, Schedletzky O, Barkemeyer J, Bargon J, Glaser SJ (1998) *J Magn Reson* 133(1):92–97
5. Duckett SB, Sleigh CJ (1999) *Prog Nucl Magn Reson Spectrosc* 34(1):71–92
6. Duckett SB, Blazina D (2003) *Eur J Inorg Chem* 2003(16):2901–2912
7. Koptuyg IV, Kovtunov KV, Burt SR, Anwar MS, Hilty C, Han S-I, Pines A, Sagdeev RZ (2007) *J Am Chem Soc* 129(17):5580–5586

8. Kovtunov KV, Beck IE, Bukhtiyarov VI, Koptyug IV (2008) *Angew Chem Int Ed* 120(8):1514–1517
9. Kovtunov KV, Zhivonitko VV, Corma A, Koptyug IV (2010) *J Phys Chem Lett* 1(11):1705–1708
10. Bouchard LS, Burt SR, Anwar MS, Kovtunov KV, Koptyug IV, Pines A (2008) *Science* 319:442–445
11. Bouchard L-S, Kovtunov KV, Burt SR, Anwar MS, Koptyug IV, Sagdeev RZ, Pines A (2007) *Angew Chem Int Ed* 119(22):4142–4146
12. Goldman M, Jóhannesson H (2005) *C R Phys* 6(4–5):575–581
13. Goldman M, Jóhannesson H, Axelsson O, Karlsson M (2005) *Magn Reson Imaging* 23(2):153–157
14. Reineri F, Viale A, Giovenzana G, Santelia D, Dastrù W, Gobetto R, Aime S (2008) *J Am Chem Soc* 130:15047–15053
15. Dechent JF, Buljubasich L, Schreiber LM, Spiess HW, Münnemann K (2012) *Phys Chem Chem Phys* 14(7):2346
16. Haake M, Natterer J, Bargon J (1996) *J Am Chem Soc* 118(36):8688–8691
17. Sengstschmid H, Freeman R, Barkemeyer J, Bargon J (1996) *J Magn Reson Ser A* 120(2):249–257
18. Jóhannesson H, Axelsson O, Karlsson M (2004) *C R Phys* 5(3):315–324
19. Ivanov KL, Yurkovskaya AV, Vieth H-M (2008) *J Chem Phys* 128:154701
20. Korchak SE, Ivanov KL, Yurkovskaya AV, Vieth HM (2009) *Phys Chem Chem Phys* 11:11146
21. Buljubasich L, Franzoni MB, Spiess HW, Münnemann K (2012) *J Magn Reson* 219:33–40
22. Carravetta M, Johannessen O, Levitt M (2004) *Phys Rev Lett* 92(15):153003–153004
23. Carravetta M, Levitt MH (2004) *J Am Chem Soc* 126(20):6228–6229
24. Carravetta M, Levitt MH (2005) *J Chem Phys* 122(21):214505
25. Jonischkeit T, Bommerich U, Stadler Jr, Woelk K, Niessen HG, Bargon J (2006) *J Chem Phys* 124(20):201109
26. Canet D, Bouguet-Bonnet S, Aroulanda C, Reineri F (2007) *J Am Chem Soc* 129:1445–1449
27. Vinogradov E, Grant AK (2008) *J Magn Reson* 194(1):46–57
28. Franzoni MB, Buljubasich L, Spiess HW, Münnemann K (2012) *J Am Chem Soc* 134(25):10393–10396
29. Anwar M, Blazina D, Carteret H, Duckett S, Halstead T, Jones J, Kozak C, Taylor R (2004) *Phys Rev Lett* 93(4):040501–040504
30. Anwar M, Xiao L, Short A, Jones J, Blazina D, Duckett S, Carteret H (2005) *Phys Rev A* 71(3):032327–032306
31. Anwar MS (2005) NMR quantum information processing with parahydrogen. arXiv:quant-ph/0509046v1
32. Hübler P, Bargon J, Glaser SJ (2000) *J Chem Phys* 113(6):2056
33. Green RA, Adams RW, Duckett SB, Mewis RE, Williamson DC, Green GGR (2012) *Prog Nucl Magn Reson Spectrosc* 67:1–48
34. Heitler W, London F (1927) *Zeitsch Phys* 44:455–472
35. Pauling L, Wilson EB Jr (1935) *Introduction to quantum mechanics, with applications to chemistry*, New edition. Dover, Mineola, New York, United States
36. Bowers CR (2007) Sensitivity enhancement utilizing parahydrogen. In: Harris RK (ed) *Encyclopedia of magnetic resonance*. Wiley, Chichester
37. Sakurai JJ, Tuan SF (1994) *Modern quantum mechanics*. Addison Wesley, Boston, United States
38. Dennison DM (1927) *Proc R Soc Lond A Math Phys* 115(771):483–486
39. Bonhoeffer KF, Harteck P (1929) *Die Naturwissenschaften* 17(11):182
40. Jonischkeit T, Woelk K (2004) *Adv Synth Catal* 346(8):960–969
41. Silvera I (1980) *Rev Mod Phys* 52(2):393–452



42. Canet D, Aroulanda C, Mutzenhardt P, Aime S, Gobetto R, Reineri F (2006) *Concept Magn Reson A* 28A:321–330
43. Natterer J, Bargon J (1997) *Prog Nucl Magn Reson Spectrosc* 31(4):293–315
44. Levitt MH (2008) *Spin dynamics: basics of nuclear magnetic resonance*, 2nd edn. John Wiley and Sons Ltd, Chichester, United Kingdom
45. Bowers CR, Weitekamp DP (1986) *Phys Rev Lett* 57(21):2645–2648
46. Ernst RR, Bodenhausen G, Wokaun A (1987) *Principles of nuclear magnetic resonance in one and two dimensions*. Oxford University Press, Published in New York United States
47. Sørensen OW, Eich GW, Levitt MH, Bodenhausen G, Ernst RR (1984) *Prog Nucl Magn Reson Spectrosc* 16:163–192
48. Abragam A (1983) *Principles of nuclear magnetism*. Oxford University Press, Published in New York United States
49. Aime S, Gobetto R, Reineri F, Canet D (2003) *J Chem Phys* 119:8890
50. Aime S, Gobetto R, Reineri F, Canet D (2006) *J Magn Reson* 178:184–192
51. Goldman M (1991) *Quantum description of high-resolution NMR in liquids*. Oxford University Press, Published in New York United States
52. Bouguet-Bonnet S, Reineri F, Canet D (2009) *J Chem Phys* 130:234507
53. Miesel K, Ivanov KL, Yurkovskaya AV, Vieth HM (2006) *Chem Phys Lett* 425(1–3):71–76
54. Theis T, Ganssle P, Kervern G, Knappe S, Kitching J, Ledbetter MP, Budker D, Pines A (2011) *Nat Phys* 7(7):571–575
55. Münnemann K, Spiess HW (2011) *Nat Phys* 7(7):522–523
56. Hoevener J-B, Chekmenev EY, Harris KC, Perman WH, Robertson LW, Ross BD, Bhattacharya P (2009) *Magn Reson Mater Phys* 22(2):111–121
57. Roth M (2010) *ArchivMeD – sensitivity enhancement in NMR by using parahydrogen induced polarization*. Roth, Meike. <http://www.ubm.opus.hbz-nrw.de/volltexte/2010/2280/>
58. Mansson S, Johansson E, Magnusson P, Chai CM, Hansson G, Petersson JS, Stahlberg F, Golman K (2006) *Eur Radiol* 16(1):57–67
59. Golman K, In't Zandt R, Lerche M, Pehrson R, Ardenkjaer-Larsen JH (2006) *Cancer Res* 66(22):10855–10860
60. Wilson DM, Keshari KR, Larson PEZ, Chen AP, Hu S, Van Crieckinge M, Bok R, Nelson SJ, Macdonald JM, Vigneron DB, Kurhanewicz J (2010) *J Magn Reson* 205(1):141–147
61. Golman K, In't Zandt R, Thaning M (2006) *Proc Natl Acad Sci USA* 103(30):11270–11275
62. Gallagher FA, Kettunen MI, Day SE, Hu D-E, Ardenkjaer-Larsen JH, In't Zandt R, Jensen PR, Karlsson M, Golman K, Lerche MH, Brindle KM (2008) *Nature* 453(7197):940–943
63. Chekmenev EY, Hoevener J, Norton VA, Harris K, Batchelder LS, Bhattacharya P, Ross BD, Weitekamp DP (2008) *J Am Chem Soc* 130(13):4212–4213
64. Roth M, Kindervater P, Raich H-P, Bargon J, Spiess HW, Münnemann K (2010) *Angew Chem Int Ed* 122(45):8536–8540
65. Acosta RH, Blümler P, Münnemann K, Spiess H-W (2012) *Prog Nucl Magn Reson Spectrosc* 66:40–69
66. Warren WS, Jenista E, Branca RT, Chen X (2009) *Science* 323(5922):1711–1714
67. Vasos PR, Comment A, Sarkar R, Ahuja P, Jannin S, Ansermet JP, Konter JA, Hautle P, van den Brandt B, Bodenhausen G (2009) *Proc Natl Acad Sci U S A* 106(44):18469–18473
68. Wild JM, Paley MNJ, Viallon M, Schreiber WG, van Beek EJR, Griffiths PD (2002) *Magn Reson Med* 47(4):687–695
69. Hu S, Lustig M, Chen AP, Crane J, Kerr A, Kelley DAC, Hurd R, Kurhanewicz J, Nelson SJ, Pauly JM, Vigneron DB (2008) *J Magn Reson* 192(2):258–264
70. Mishkovsky M, Frydman L (2008) *Chemphyschem* 9(16):2340–2348
71. Roth M, Koch A, Kindervater P, Bargon J, Spiess HW, Münnemann K (2010) *J Magn Reson* 204(1):50–55
72. Baumer D, Brunner E, Blümler P, Zänker PP, Spiess HW (2006) *Angew Chem Int Ed* 45(43):7282–7284

73. Amor N, Zaenker PP, Bluemler P, Meise FM, Schreiber LM, Scholz A, Schmiedeskamp J, Spiess HW, Muennemann K (2009) *J Magn Reson* 201(1):93–99
74. Jeener J (1971) Lecture notes from Ampere summer school in Basko Polje, Yugoslavia. unpublished
75. Aue WP (1976) *J Chem Phys* 64(5):2229
76. Messerle BA, Sleigh CJ, Partridge MG, Duckett SB (1999) *J Chem Soc Dalton Trans* (9):1429
77. Adams RW, Aguilar JA, Atkinson KD, Cowley MJ, Elliott PIP, Duckett SB, Green GGR, Khazal IG, Lopez-Serrano J, Williamson DC (2009) *Science* 323(5922):1708–1711
78. Toda M, Kubo R (1992) *Statistical physics. I. Equilibrium statistical mechanics*, 2nd edn. Springer, Berlin